stellarator news

Published by Fusion Energy Division, Oak Ridge National Laboratory
Building 9201-2 P.O. Box 2009 Oak Ridge, TN 37831-8071, USA

Editor: James A. Rome Issue 61 January 1999
E-Mail: jar@ornl.gov Phone (423) 574-1306 Fax: (423) 576-3647
On the Web at *http://www.ornl.gov/fed/stelnews*

Tenth Anniversary Issue

This issue of *Stellarator News* marks the start of the eleventh year of continuous, bimonthly publication. To be historically accurate, the first issue of *Stellarator News* appeared in the spring of 1983, but regular publication commenced in November 1988.

I launched the November issue with the following statement: “This is an exciting time in the stellarator community because many machines are about to start producing data in previously unreachable regimes of operation.” At that time, ATF was ending its second phase of operation, W7-AS had just started plasma operation, CHS was ending its ECH-only phase and embarking on ICRF heating, and Heliotron-E was doing pellet injection and edge plasma studies. Uragan-3M had just tested its new coils. L-2 was doing ECR heating of currentless plasmas. Already, W7-X and LHD were being designed.

Ten years later the promises of these devices have been fulfilled, and today the first stellarator experiment with a large plasma, LHD, is already producing the best results ever attained; another such device, W7-X, is being built.

Because of the great number of excellent results in worldwide stellarator research, it is easy to lose sight of the big picture. I believe that the change in the overall perception of a stellarator is important, and worthy of some examination. The next article by Masami Fujiwara gives an excellent summary of the advances of the past decade.

As we approach the new millennium, the necessary tools, experimental results, coil technology, and insights now exist to create a new generation of stellarators that promise steady-state operation, good transport, and stable operation at the beta values appropriate to a reactor. The next ten years promise to be more exciting than ever.

I wish to thank Bonnie Nestor for her outstanding efforts as Technical Editor for *Stellarator News*. Because this is an international newsletter, it is a challenging task to be sure that all articles are in good English while retaining the individual styles of the authors. I can rely upon Bonnie to clarify and sharpen the writing without changing its meaning.

James A. Rome, Editor

In this issue . . .

Progress in stellarator research and prospects for the future
Stellarator research has made great strides in theory, experiment, and concept development in the past decade. 3

Status of the Wendelstein 7-X experiment
The advanced stellarator Wendelstein 7-X is under construction at the Greifswald branch of the IPP Garching, Germany. The device will produce steady-state, reactor-relevant plasmas and test necessary technology. 6

Overview of Wendelstein 7-AS results
Wendelstein 7-AS (W7-AS), now in operation at IPP Garching, is one of a series of low-shear stellarators with successively optimized designs. W7-AS is a partly optimized stellarator. The maximum parameters achieved in W7-AS (in different discharge types) are $T_e = 5.8$ keV, $T_i = 1.5$ keV, $n_e = 3 \times 10^{20}$ m^{-3}, $\langle\beta\rangle = 2\%$, $\tau_E = 50$ ms. 8

The dependence of confinement on rotational transform and magnetic shear in Wendelstein 7-AS
Transport in the low-shear Wendelstein 7-AS depends on both the rotational transform and the shear. Transport at rational surfaces is modeled by enhanced turbulence. 13

Bifurcations of neoclassical and turbulent transport in Wendelstein 7-AS
Confinement bifurcations are observed in Wendelstein 7-AS plasmas. The maximum values of T_e, T_i, and τ_E obtained are achieved after a transition to one of the improved confinement states. An important element of the observed bifurcation processes is the radial electric field. 16

Polarimetric line density measurements at Wendelstein 7-AS using the Cotton-Mouton effect
The Cotton-Mouton effect is observed if the magnetic field is perpendicular to the direction of propagation. The capability of the Cotton-Mouton effect to provide a robust measurement of the line integrated density at Wendelstein 7-AS (W7-AS) has been demonstrated. An optimized set-up is proposed for W7-X. Both W7-X and W7-AS offer a favorable magnetic field topology for the method. 19

Recent results with ECRH and ECCD on the Wendelstein 7-AS stellarator
Experiments with ECRH and ECCD were performed at Wendelstein7-AS with enhanced heating power, extending well beyond the previous frame of investigations. The central confinement of ECR-heated discharges is strongly influenced by ECRH-specific features. Positive radial electric fields driven by fast electron losses in the plasma center (electron root) provide significantly enhanced electron confinement, resulting in peak temperatures of 5.7 keV. Net current-free discharges with up to 20 kA of highly localized EC-driven currents in the co- and counter-direction to the bootstrap current were investigated and compared with linear predictions. The radial profile of the rotatational transform was tailored by strong ECCD over a wide range. 22

Electron Bernstein wave heating and emission via the OXB process at Wendelstein 7-AS
Access to overdense plasmas ($n_e > n_{e,cut-off}$) for both electron Bernstein (EB) wave heating and the EB wave diagnostic via the OXB mode conversion window has been successfully demonstrated at W7-AS. 25

Computational study of toroidal Alfvén eigenmodes in W7-AS
W7-AS diagnostics can produce precise information on the frequencies as well as the spatial structures of MHD activities in the plasma. The CAS3D code accurately models the experimental results. 30

Energetic particle-driven Alfvén instabilities in W7-AS
Neutral-beam-driven Alfvén eigenmodes are the most striking MHD instabilities in W7-AS, and therefore continuous efforts are made to study their characteristics and their relevance for fast particle confinement. The low shear causes toroidal Alfvén eigenmodes (TAE) gaps to disappear and results in the appearance of weakly damped global Alfvén eigenmodes (GAEs) below the Alfvén continua with frequencies $\omega_{GAE} = (k_{||} \cdot v_A)_{min}$, which are excited through resonances with fast passing particles from NBI. The low-frequency coherent Alfvén modes do not cause significantly increased losses. These modes are typically observed under conditions with $v_A > v_{beam}$, where only sideband excitation is possible. With increasing beam power and density, however, strong bursting mode activity occurs with frequencies up to 500 kHz, which can induce significant energy and particle losses. 32

Island divertor studies for Wendelstein 7-AS
Basic features of the island divertor concept for low-shear stellarators are briefly reviewed. A realistic treatment of the 3-D plasma edge transport in the island divertor has become possible by the development of the EMC3 code. Recently the code has been applied to high density “detachment-like” conditions with temperatures down to 1 eV at the targets. By increasing the density, the ionization front is shown to shift gradually from the target to the separatrix. Cross-field diffusion is predicted to cause strong momentum losses even for low recycling conditions due to the small poloidal and radial extent of the divertor region in W7-AS. 34

Quasisymmetries in toroidal confinement
Because orbits in currentless stellarators depend only on the magnitude of ***B***, symmetries can be achieved in *B* even though the vector field is fully three-dimensional. *B* can exhibit quasihelical, quasiaxisymmetric and quasi-isodynamic symmetries which yield configurations with greatly improved transport properties. 36

Design studies of low-aspect-ratio quasiomnigeneous stellarators
Significant progress has been made in the development of new modest-size compact stellarator devices that could test optimization principles for the design of a more attractive reactor. These are 3- and 4-field-period low-aspect-ratio quasiomnigeneous stellarators based on an optimization method that targets improved confinement, stability, ease of coil design, low aspect ratio, and low bootstrap current. 38

Progress in stellarator research and prospects for the future

Background

Great progress in fusion reactor research has been made during the last decade, supported by active research on tokamaks, helical systems, reversed-field pinches (RFPs), and other configurations. On one hand, the tokamak effort has lead to the design of an ignition experiment, the International Thermonuclear Experimental Reactor. On the other hand, investigations of helical systems (stellarators, heliotrons/torsatrons, heliacs, etc.) have reached a level that supports the development of improved reactor designs, and operation of experiments that have entered into the high temperature plasma regime.

The motivation for the original concept of the stellarator was to realize quiescent fusion plasmas in a magnetic configuration in which magnetic field lines, being produced by external coils, form closed and nested toroidal surfaces. This is quite different from but very advantageous in comparison with other configurations such as the tokamak, RFP, or spheromak in which an electric current flows inside the plasma to form the confining magnetic field.

However, nature does not bless us so easily, and various difficulties with the stellarator concept were discovered in the early stages of fusion research. First of all, helical configurations have helical symmetry only in the limit of linear and straight devices, and the symmetry is broken in toroidal geometry. As a consequence, the stellarator concept was hampered by the appearance of a loss cone for particle confinement and by enhanced transport due to helical ripple fields. Such losses appear in addition to the usual toroidicity-enhanced collisional transport and turbulence-driven losses which are related to various instabilities. Another obstacle was perceived to be the complicated structure of helical systems which has made it difficult to construct larger, high-field experimental devices with the necessary high accuracy.

Researchers in the stellarator community have made great efforts in developing experiment and theory to identify helical systems that could realize the potential advantages of the stellarator concept. Studies started at a very preliminary level, using small-scale devices such as Heliotron-D, Wendelstein IIb, and JIPP-I, and then were extended to the medium-scale devices Heliotron-E (H-E), Wendelstein VII-A (W7-A), the Compact Helical System (CHS), and the Advanced Toroidal Facility (ATF). The progress in these studies finally led to the construction and operation of the Large Helical Device (LHD) in this decade.

The plasma parameters have been also gradually improved with increases in machine scale, with successful application of heating, and with the elaboration of the understanding of the complex plasmas. The parameters started with temperatures of 10–100 eV and a confinement time of $\tau_E \sim$ 1 ms in small devices two decades ago. In this decade, they have reached the multi-keV range of temperature (T_e ~ 6 keV in high-power ECH discharges on W7-AS) and τ_E of the order of 10 ms. The most recent results obtained in LHD experiments are $T_e \sim 2.5$ keV, $T_i \sim 2$ keV, and $\tau_E \sim$ 200 ms, and the discharge duration has reached more than 20 s. A recent photograph of LHD is shown in Fig. 1.

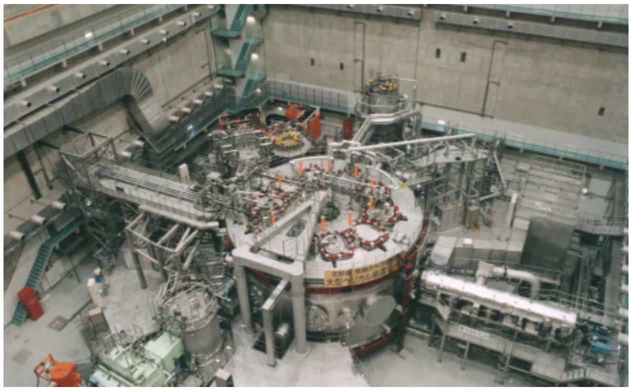

Fig. 1. The Large Helical Device in Toki, Japan.

Progress in confinement physics

1. By means of an intensive international collaboration, an empirical scaling law known as ISS95 has been established for the global confinement time of plasmas in medium-size helical systems. A similar dependence on heating power, density and magnetic field has been found

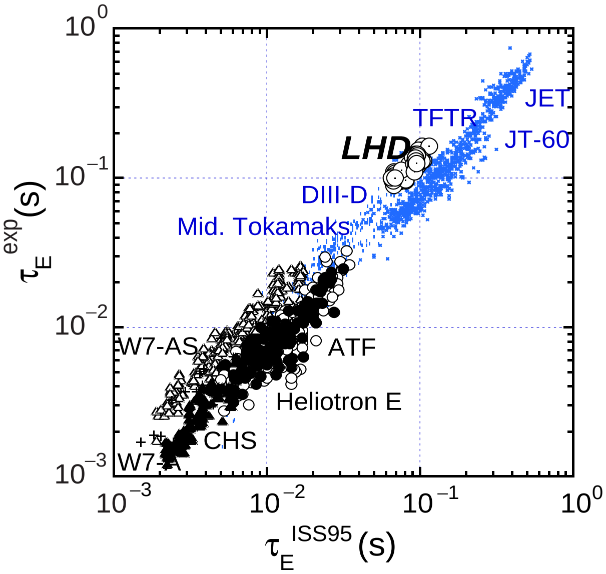

Fig. 2. ISS95 scaling for the energy confinement time of stellarators and tokamaks.

among the various types of helical systems. ISS95 has a similar form to tokamak L-mode scaling, with features common to several scaling laws (LHD, Lackner-Gottaldi, and others). The power degradation of the confinement time has been identified as a key issue to be resolved in the future. However, at the same time, the rate of degradation with respect to heating power is close to that in tokamaks. ISS95 scaling is shown in Fig. 2, including recent LHD data.

2. Plasmas in a long-mean-free-path (LMFP) regime have been realized without encountering a possible predicted stronger degradation of the confinement time due to the ripple-trapped particle loss. The latter loss has long been a concern for non-axisymmetric devices, but it was not so strong as to prohibit the achievement of the LMFP regime.

3. Experimental findings of various kinds of improved modes have been reported in this decade; e.g., H-mode-like operation in W7-AS, CHS, and H-1; high-T_i mode operations in CHS and H-E; high-confinement NBI mode in W7-AS; and the internal transport barrier in CHS. The establishment of the H-mode in various kinds of helical systems shows, on one hand, that the transition at the edge is an intrinsic feature of toroidal plasmas. On the other hand, the H-mode characteristics are also quite sensitive to the edge geometry and divertor field line structure. The high-T_i mode experiments have emerged from successful density profile control. These observations clarify the key requirement for control of the edge plasma and the density in the steady-state plasmas of the coming decade.

4. The global MHD equilibrium is very well understood in several devices. The observation of the axis shift (Shafranov shift) dependence on the plasma beta is well explained by theory in CHS, W7-A, H-E and W7-AS. In particular, the reduction of the toroidal shift in the W7AS experiment clearly demonstrated the validity of the concept of an optimized advanced stellarator configuration.

Another key issue in the MHD equilibrium is the determination of the structure near rational surfaces. Theoretical studies have shown the possibility of a magnetic island caused by the pressure gradient. Experiments on W7-AS, a low-shear helical system, indicate an increment of transport at rational surfaces. Identification of the plasma nature near the rational surfaces is left for study in the next decade.

5. Plasma beta has been increased substantially in this decade. The highest beta was achieved in CHS, $\langle\beta\rangle \sim 2.1\%$ and $\beta(0) \sim 7.5\%$ in stable discharges. Pressure-gradient-driven events and internal disruption have been observed on H-E for a particular shape of plasma pressure profile. So far, however, the achieved beta in CHS and W7-AS is limited by the amount of heating power, not by a violent beta-limiting event.

The physics of Alfvén eigenmodes, excited by energetic particles in high-beta plasmas, has also advanced. Experimental studies of toroidal Alfvén eigenmodes on W7-AS would be the most precise among toroidal plasma experiments. Such modes have been identified in high-beta plasmas, but they remain weak so far, and no strongly deteriorating effect has been observed.

6. The density limit is experimentally indicated to be much relaxed in helical devices compared with tokamaks. The limit is 2–3 times the Greenwald limit of an equivalent tokamak when the rotational transform is converted to the equivalent plasma current. The identification of the rule that governs the density limit is an important future task, because the best fusion triple product, $Tn\tau$, would be reached near the density limit.

7. The physics concerned with plasma potential and radial electric fields has advanced greatly. Emphasis has been placed on the reduction of neoclassical transport in non-axisymmetric stellarator configurations. At the same time, the electric field plays important roles in causing the H-mode transition and suppressing turbulence by $\boldsymbol{E} \times \boldsymbol{B}$ sheared flow, as in tokamaks. In helical systems, the neoclassical transport can cause strong current across the magnetic surfaces, and a variety of bifurcation phenomena are expected to occur. Measurements of plasma rotation, by use of charge exchange recombination spectroscopy (CXRS) and direct measurements of plasma potential with a heavy ion beam probe (HIBP) are gradually clarifying the relationship of improved confinement modes, plasma profile, and rotation. This area of study has led to the identification of an internal transport barrier (and the suppression of turbulence at the barrier) in CHS.

Another important and quite new phenomenon has been discovered in CHS experiments: dramatic pulsations in the potential of the entire plasma (Fig. 3). This phenomenon is found in helical plasmas and indicates a transition between two bifurcated stable states depending on the balance of ion transport and electron transport, which are deeply coupled to the radial electric field. This phenomenon not only provides new insight into the physics of structure formation in toroidal plasmas, but also demonstrates a new aspect of a “steady-state plasma” confined by a static external magnetic field.

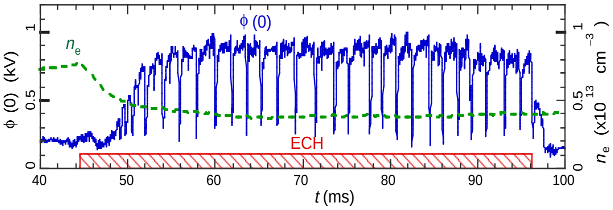

Fig. 3. Electric potential pulsation phenomenon exhibited by CHS.

Developments in device and plasma technologies

Advances during the last decade in technologies for device construction and operation make it possible to construct larger-scale and higher-field devices with high mechanical and magnetic field accuracy. As shown in Table 1, the scale, plasma volume, and magnetic field strength have increased gradually from R = 1–2 m, V_p ~ 1–2 m^3, and B ~ 2 T in the last decade to R ~ 4 m, V_p ~ 30 m^3, and B ~ 3 T in LHD and W7-X. Heating power has also increased from ~1 MW to 20 MW. Table 1 gives the machine parameters of several helical devices. The discharge duration of plasmas was about 1 s because almost all devices used copper coils. A most significant advance was made on LHD by employing superconducting (SC) coils and long-pulse heating; this system has already demonstrated 20-s plasma operations.

Table 1. Parameters of recent stellarators

Device name	R (m)	a_p (m)	V_p (m^3)	B (T)
L2-M	1.0	0.11	0.24	1.5
U-3M	1.0	0.13	0.33	2.0
U-2M	1.7	0.22	1.6	2.4
H-E	2.2	0.2	1.7	2.0
W7-A	2.0	0.1	0.39	3.5
ATF	2.1	0.3	3.7	2.0
H-1	1.0	0.2	0.79	1.0
CHS	1.0	0.2	0.79	2.0
W7-AS	2.0	0.2	1.6	2.5
CAT	0.53	0.1	0.10	0.1
TJ-IU	0.6	0.1	0.12	0.7
TJ-II	1.5	0.2	1.2	1.0
HSX	1.2	0.15	0.53	1.25
LHD	3.9	0.6	28	3.0
W7-X	5.5	0.5	27	2.5

Coil and magnet technology has also made great progress in this decade. A modular coil system has been constructed at W7-AS with good accuracy and 2.5-T field, and TJ-II was also completed as a combination of spatially arrayed toroidal coils surrounding a set of central ring conductors.

On LHD NbTi SC conductor was used for the pool-boiling helical coil. The continuous helical winding was designed to provide a “clean” helical divertor field structure for particle and heat control. The poloidal coils (NbTi cable-in-conduit type conductor) employ forced-flow cooling. The helical coil, with 450 turns of SC conductor (36 km), was wound with a positional error of less than 2 mm. Stable operation has now been demonstrated at 2.75 T.

Advances in cooling technology have also been implemented on LHD. This large-scale machine (R = 4 m) contains 1 GJ stored energy in its SC magnets, which represents a total weight to be cooled of 900 tonnes including the magnet supporting structure. In particular, high-level control of the cooling was successfully demonstrated to keep the temperature difference less than 50 K during cooldown to reduce thermal stress.

The plasma production and heating scheme in helical devices is usually ECH, NBI, or ICRF heating of ECH-generated plasmas; this is slightly different from tokamaks and others, in which an initial plasma is produced by Ohmic heating due to plasma current and then heated by NBI or ICRF. The technology of long-pulse heating methods for helical systems have also been developed during the last decade. For high-power ECRH gyrotrons, the capability reaches ~200 GHz, 1 MW, and 10 s/tube. For NBI using a negative ion source, the power level reaches 7.5 MW/injector with 180 keV(H) in LHD. For ICRF, the power and pulse length are 3 MW and 30 min in case of oscillator/transmission test.

Advances in concept development

Concept development in stellarators tries focuses on finding optimized configurations to confine high-temperature collisionless plasmas at higher stable betas, in a regime relevant to fusion plasmas, together with divertor structures (as compact as possible) to handle particle and heat control. Planar-axis helical devices such as W7-A, JIPPT-II, H-E, ATF, CHS, and LHD, which employ continuous helical windings and toroidal coils, were optimized by (1) adjusting the pitch of helical coils, (2) using various poloidal fields to control the position of the magnetic axis and the shape of the cross section, creating possibilities for the control of the magnetic well/shear and bootstrap current as well as for the reduction of ripple-loss, and (3) forming a “clean” helical divertor field line structure.

For spatial-axis helical devices, in addition to heliac-type configurations such as H-1 and TJ-II, a rather new way of thinking or principle for configuration development has been developed. The process starts by developing an optimized configuration for the magnetic structure in the core plasma region, and the analysis is continued to find a coil design, in particular, modular coils, to realize a required magnetic configuration. This method has been successfully demonstrated by the W7-AS device and has been extended to W7-X design. The concept of W7-X is to make a magnetic configuration in which the response of the plasma-like Pfirsch-Schlüter current or bootstrap current is minimized and the ripple transport is also much reduced.

This approach has lately been developed further, and new types of configurations have been obtained [see J. Nührenberg, "Quasisymmetries in toroidal confinement," in this issue]. The first is so-called *quasihelical symmetry*, which has good helical symmetry, close to being a linear stellarator, even though the mechanical aspect ratio is finite. For example, in HSX (University of Wisconsin, Madison), the effective aspect ratio which plasma particles experience is 500 while the actual mechanical one is 11. The plasma is expected to behave as if it were in a linear stellarator. The second one is *quasiaxisymmetry* (QA), in which the effective helical ripple is negligibly small and the rotational transform of magnetic field line is finite enough for plasma confinement. The rotational transform arises mostly from the bootstrap current. In this respect, QA is close to a steady-state, bootstrap current driven tokamak without current disruption.

These concept developments are based on the nature of particle orbits in a vacuum field or on collisional transport. It has now become clear that the collective plasma response, such as turbulent transport or electric field structure formation, plays a decisive role in the confinement of helical plasmas. Control of the electric field structure is the key for the improvement of confinement, as has been verified in the achievement of the internal transport barrier, and possibly the beta limit. Concept development in the next decade will be extended on the basis of the dramatic evolution of the understanding of plasmas in this decade.

Summary

Experimental and theoretical studies of plasma confinement in helical devices have led to significant progress in this decade on the devices TJ-IU, L-2M, U-3M, W7-A, ATF, H-E, CHS, W7-AS, and the newly commissioned TJ-II and LHD. The physics has been advanced, and results complementary to those obtained in tokamaks have been developed. The research has brought enrichment to the understanding of toroidal plasmas in general.

The technologies required for stellarators have also been developed. Magnet technologies are in hand, as represented by the SC helical coils of LHD, by the modular coils of W7-AS, and by special coil fabrication in TJ-II, H-1, and others. In heating methods, NBI, ECH, and ICRF have been developed to the level of several megawatts of power and several seconds in duration.

In the coming decade, LHD will generate quite important data by its full operation with higher temperature, long-pulse/steady-state plasmas; W7-X will be completed and in operation; and other devices will also develop basic key physics and technologies to realize a steady-state fusion reactor. Experimental and theoretical studies will play a leading and propelling role for fusion research and for fusion science.

Masami Fujiwara
National Institute for Fusion Science
Toki, Japan

E-mail: fujiwara@nifs.ac.jp

Status of the Wendelstein 7-X experiment

The advanced stellarator Wendelstein 7-X (W7-X) is under construction at the Greifswald branch of the Institut für Plasmaphysik (IPP) Garching, Germany. The physics goals for W7-X can be summarized as follows:

- Demonstration of steady-state operation in a reactor-relevant plasma parameter regime.
- Demonstration of good plasma confinement to improve the database for reactor extrapolation.
- Demonstration of stable plasma equilibrium at a reactor-relevant plasma $\langle\beta\rangle$.
- Investigation and development of a reactor relevant divertor.

The physics objectives have direct consequences for the design of W7-X. Steady-state operation (typically 30 min at first) demands superconducting coils, a continuously operating heating system, and an actively cooled divertor. In addition, provisions for the integration of next-generation divertor structures must be made. The technical data of W7-X are summarized in Table 1.

Various engineering aspects of the device have been described in previous issues of *Stellarator News* (Issue 39: Engineering aspects of W7-X; Issue 42: Superconductor development; Issue 47: W7-X diagnostics; Issue 51: Divertor aspects; Issue 59: DEMO cryostat). Meanwhile, important progress has been made in the development program and the procurement of main components of the basic device.

The development program consists of prototype work on the superconductor, the nonplanar coils, the cryostat, the ECRH gyrotrons, and the plasma-facing components. The procurement plan is being pursued along the critical path of the project, starting with the magnet system and the cryostat.

The superconductor for W7-X will be a NbTi cable-in-conduit conductor. Based on the positive tests of a basic version of the conductor, as described in Issue 42, an

Table 1. Characteristic data of W7-X

Machine diameter	16 m
Total height	5 m
Weight	550 t
Major plasma radius	5.5 m
Minor average plasma radius	0.53 m
Plasma volume	30 m^3
Number of nonplanar/planar coils	50/20
Magnetic field on the axis	3 T
Heating power (first/second stage)	15/30 MW
Plasma pulse length	10 s, with full-power continuous operation at 10 MW of ECRH

"advanced conductor" was built and successfully tested. This conductor is characterized by the following parameters:

- The strands are 0.59 mm in diameter and are made of 144 NbTi filaments with a diameter of 26.1 µm embedded in a copper matrix (Cu:NbTi = 2.56:1). The critical current of the strands amounts to >190 A at 6 T and 4.2 K.
- The cable ~12 mm-diam of is composed of 243 strands wound in triplets and has a void fraction of 36.5%.
- The final conductor has a cross section of 16 × 16 mm^2. The cable is jacketed by an alloy, $AlMgSi_{0.5}$, which can be hardened after winding.

The conductor was tested in the STAR facility at the Forschungszentrum Karlsruhe (FZK) as described in Issue 42. The conductor reached a critical current of 22.5 kA at a field of 7.4 T and a temperature of 4.6 K; this means a safety factor of 2 with respect to the critical current or a temperature margin of >1.3 K for the nominal parameters of W7-X. In addition, the conductor could bear ac losses of up to 16 mW/m at 16 kA, 5.3 T, and 4.7 K without problems. These ac losses are far in excess of the W7-X design value of 6 mW/m. Based on these positive results, the nominal number of 120 turns in the nonplanar coils was reduced to 108, still fulfilling the safety margins as specified in the original design. This reduces the cost for coil manufacturing and gives more space for the coil housing. The major problems for the manufacturing of the conductor are the proper cabling of the strands and the cladding with the aluminum alloy. Further optimization of the manufacturing process will be pursued during the construction of the nonplanar coils.

Another essential part of the prototype program for W7-X is the construction of the DEMO coil. This is a full-size, nonplanar coil featuring all the characteristics of the coils for W7-X. This coil was ordered from the German company Preussag-Noell at Würzburg with Ansaldo/Italy as subcontractor for the winding pack. The winding pack was delivered to Noell at the end of 1997. There it was embedded into the coil casing. Special emphasis was given to establishing a prestress between the stainless steel casing and the aluminum conductor at room temperature. This is necessary to obtain an almost stress-free state at 4 K, given the different thermal expansion coefficients of the winding and the casing. Figure 1 shows the winding pack inserted into the lower half of the coil casing. Detailed descriptions of the manufacturing of the coil can be found in the proceedings of the 20th Symposium on Fusion Technology (Marseilles, 1998).

The coil was mechanically completed and instrumented with sensors for temperature and strain measurements and delivered to FZK in summer 1998. The coil will be tested in the TOSKA facility, using the EURATOM LCT coil to produce the background field. After the coil is tested at nominal parameters, it will be subjected to overload conditions of more than 120% of the expected forces and stresses. The tests will start early in 1999.

The DEMO cryostat, which is also being built by industry (Balcke-Dürr Company in Ratingen, Germany), is in the final stage of assembling at IPP, as described in Issue 59. Presently the time-consuming manual work of assembling the thermal insulation and the 80 K shield is being performed. This work is expected to be finished by spring 1999 and will be followed by a comprehensive cryogenic test.

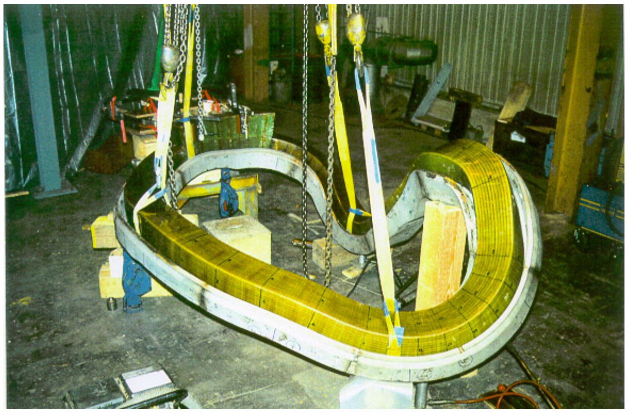

Fig. 1. Winding pack of the DEMO coil inserted into the lower-half of the coil casing.

The ECRH system for W7-X will be designed, developed, and installed by FZK in collaboration with IPF Stuttgart. For the development of gyrotrons with an output power of 1 MW at 140 GHz and cw operation, a collaboration with Thomson Tubes Electroniques was established.

In parallel to the R&D activities, the detailed design of the 50 nonplanar and 20 planar coils for the W7-X device was carried out. The design had to consider various physical boundary conditions: magnetic field structure, sufficient distance from the vacuum vessel and the ports, adaptation to the intercoil structure, and coil support. The tender for the nonplanar coils started in April 1998 and was finished by the signature of the contract with the consortium Noell/Ansaldo on 18 December 1998.

For the planar coils, the tender action started four months later. Competitive offers have been received. Following technical evaluation, negotiations have started. With the two contracts for the coil system, almost 50% of the budget for the construction of W7-X will be committed. For the acceptance tests of the W7-X coils, an agreement was made with the low-temperature institute at CEA Saclay.

In spring 1999, the W7-X construction team will move to Greifswald. At Greifswald, the construction of the buildings for the experiment and the office space is progressing well, as described in Issue 59.

J.-H. Feist and M. Wanner for the W7-X Construction Team
Max-Planck-Institut für Plasmaphysik
EURATOM Association
D-85748 Garching, Germany

E-mail: feist@ipp.mpg.de
Phone +49-89-3299-1607

Overview of W7-AS results

The Wendelstein stellarator program of Garching has developed low-shear stellarators with successively optimized designs to remove the intrinsic deficiencies of this three-dimensional (3-D) concept. W7-AS, the presently operated device, is a partly optimized stellarator. The optimization of stellarators aims at improved neoclassical confinement in the long mean-free-path regime and improved equilibrium and stability. In this report, we address equilibrium, stability, turbulent and collisional energy confinement, particle transport, high-density operation, the development of the island divertor for exhaust, and rf heating. The maximum parameters achieved in W7-AS (in different discharge types) are $T_e = 5.8$ keV, $T_i = 1.5$ keV, $n_e = 3 \times 10^{20}$ m^{-3}, $\langle\beta\rangle = 2\%$, $\tau_E = 50$ ms.

The W7-AS device

W7-AS has the form of a pentagon and its field structure is partly optimized ($\langle j_{\parallel}^2\rangle/\langle j_{\perp}^2\rangle = 0.85/\iota\!\!\!-(a)^2$). The field system is composed of modular coils [$\iota\!\!\!-(a) = 0.4$]. Toroidal field coils allow changes of $\iota\!\!\!-(a)$, and vertical field coils allow variation of the radial plasma position. W7-AS is also equipped with an Ohmic heating (OH) system that is used, for example, to compensate for the bootstrap current. In addition, the magnetic field strength in the corners of the pentagon can be varied (variation of mirror ratio). The bootstrap current is tokamak-like and the rotational transform increases; generally, operation is such that a superimposed inductive current cancels this increase of the edge rotational transform to maintain the pre-set value. Shear can be varied with OH current and by electron cyclotron current drive (ECCD). The vertical field allows change of the magnetic well and thus modifies stability properties. In addition, it allows changes of the interaction between the plasma and the 5×2 array of graphite tiles mounted symmetrically on the inboard walls. Recently, 5×2 control coils have been inserted into the vessel to allow variation of the higher Fourier components of the field with the effect that the natural islands used to divert the scrape-off layer (SOL) fluxes can be radially increased or smoothed, and thus the connection length within the island can be varied.

Equilibrium properties

The optimization of W7-AS has been demonstrated by indirect measurement of the parallel currents $\langle j_{\parallel}^2\rangle$, which were found to be reduced, as expected, and by the demonstration of reduced Shafranov shift in high-β equilibria in comparison to a classical $\ell = 2$ stellarator. Maximum $\langle\beta\rangle$-values close to 2% have been reached on W7-AS; limited by restricted heating power at given radiation losses. High-β operation is carried out at low field, $B = 1.25$ T, and at high density. Under these conditions, orbit losses are pre-

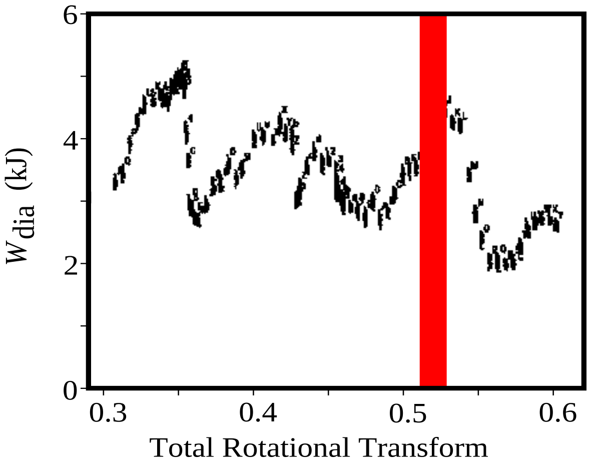

Fig. 1. Diamagnetic energy as a function of rotational transform in W7-AS. The stored energy is highest near, but not at, the rational surfaces.

dicted for energetic particles injected by the counter-injecting beam line. The increase in β with NBI is found to be mainly due to the co-injected beams. The additional increment in β achieved with the counter-injected beams is small. The high-β program on W7-AS will be continued by reversing the counter- injector into the co-direction. Under these conditions, it is expected that β will be limited by resistive interchange.

Stability properties

The high-β plasmas of W7-AS are rather quiescent and reach stationary phases until the heating is turned off. No violent MHD processes occur in the high-β phase. With a low-order rational surface in the plasma core, a pressure-driven mode may appear; it rotates in the electron drift direction at a few kilohertz and does not reduce the energy content of the plasma. With plasma current — either bootstrap current or current induced by OH or ECCD — current-driven tearing modes can appear due to resonances. Their impact on the plasma depends on the current level. Although the plasma does not disrupt, the current-induced formation of tearing mode islands causes the irreversible loss of a major part of the energy content. A current-induced rise in ɨ(a) by Δɨ ~ 0.2 is sufficient, if ɨ(a) = 0.5 is reached, to expel 80% of the energy content.

The most conspicuous MHD feature of W7-AS is global Alfvén eigenmodes (GAEs), which are driven by that part of the fast particle spectrum which is in resonance. In case of sideband excitation (m ±1), particle velocities down to $v_A/10$ can contribute. GAEs appear typically in the absence of a rational ɨ in the plasma; in the low-shear case of W7-AS, their frequency resides closely below the corresponding continuum band. The frequency varies with density, isotope mass, and field in the expected form. The GAE modes generally saturate at a level up to $\delta B/B \sim 10^{-4}$; there is no evidence, at present, that they limit the NBI heating efficiency (locally or globally).

Confinement

Low vacuum-field shear is a design characteristic of the Wendelstein line. The idea behind low shear is that low-order resonances arising from the mode spectrum of the magnetic field as well as from external field perturbations should be avoided because they reduce the energy content by the supporting development of magnetic islands. The most obvious experimental evidence is that, in the accessible ɨ range of W7-AS, good confinement (e.g., the H-mode) is established in the vicinity of ɨ(a) = 1/2 and 1/3 where larger ɨ intervals free of resonances occur, see Fig. 1. (Empirically, it is found that resonances beyond $m = 20$ have no influence.) There is ample experimental evidence that demonstrates the sensitivity of confinement to ɨ(a). At low shear, confinement can be “good” but, without further means, it is at the L-mode level (e.g., in the window ɨ(a) = 0.50–0.53. Outside this range, the confinement is at a sub-L-mode level. As described below, confinement can be increased to the H-mode level in the favorable ɨ windows.

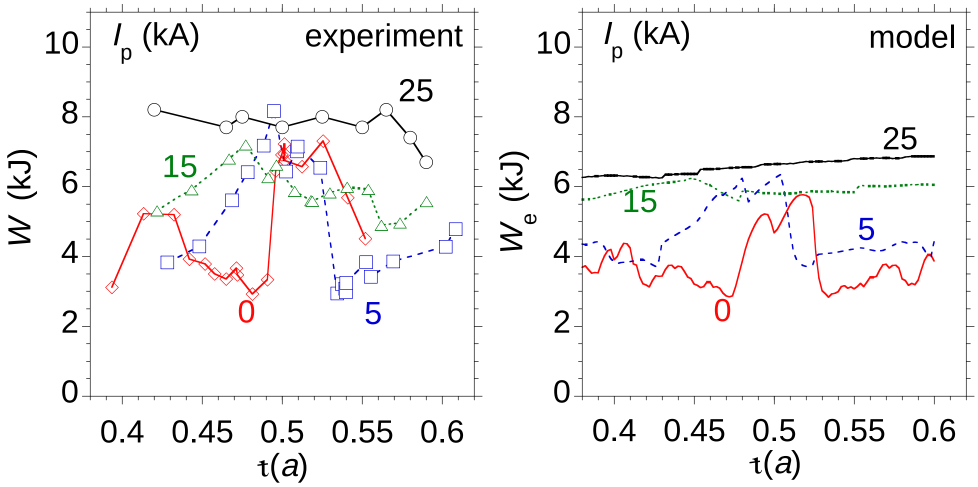

Fig. 2. Experimental variation of the energy content W with ι(a) with the plasma current I_p as a parameter. The right side shows the modeled dependence of the electron energy content W_e.

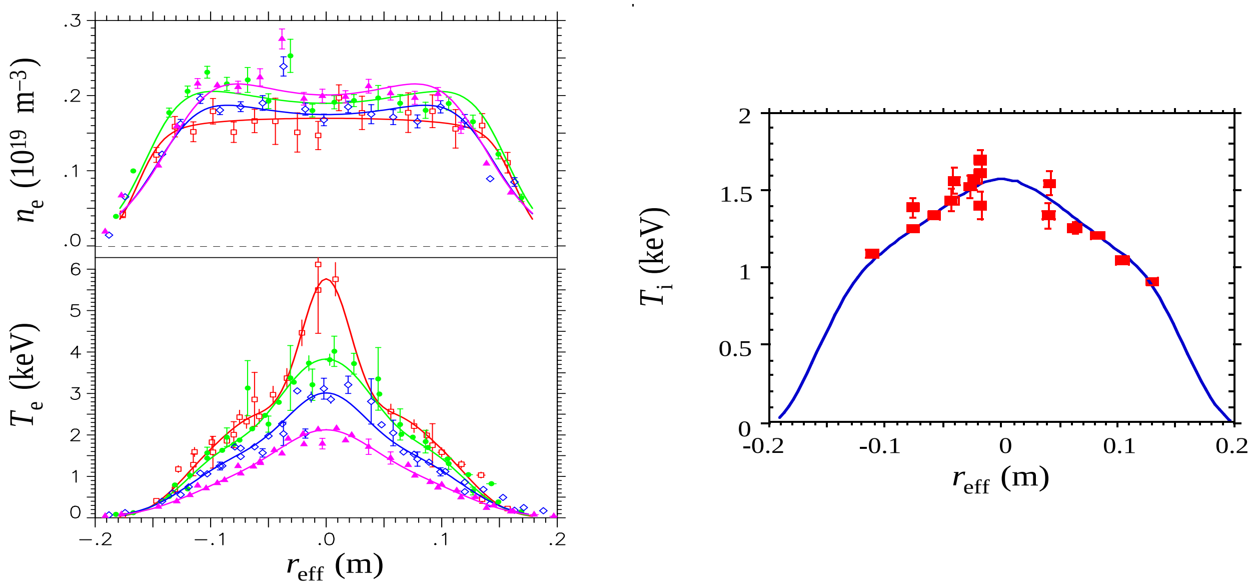

Fig. 3. Left: ECRH power scan leading to the highest electron temperature. Right: highest ion temperature on W7-AS (see text).

The impact of resonances on transport can be modeled in terms of the electron heat diffusivity, which has three components: the neoclassical χ_{neo}; the anomalous χ_{an}, which describes the good confinement (L-mode level); and an additional $\Sigma\chi_{nm}$, which represents the contribution of the resonances. The view is that resonances do not necessarily cause islands, which short-circuit a small radial range, but rather give rise to locally enhanced turbulence. The χ_{nm} term is parameterized by an amplitude a_{nm}, a radial range of effectiveness, and a damping factor which itself depends on shear. Three fitting parameters are determined from confinement results in experimental scans which allowed χ_{nm} to be varied. Figure 2 compares the experimentally measured variation of the energy content W with $\iota\!\!\!-(a)$ at different plasma currents (shear values), and compares it to the modeling results for W_e.

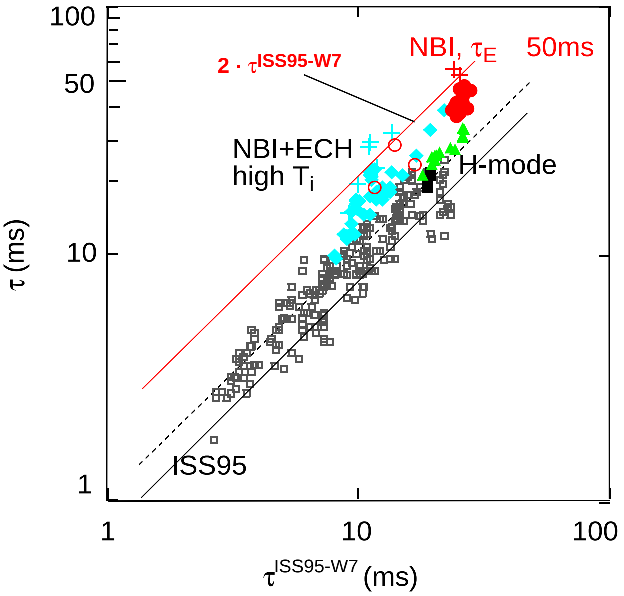

Fig. 4. Standard “L-mode” data of W7-AS and τ_E of enhanced regimes in comparison to the ISS95 scaling.

Neoclassical core transport

In cases of improved confinement, the core electron temperature rises and because of the strong T_e dependence of Q_{neo} [$\sim T_e^{9/2}$ (without E_r)], the core confinement becomes neoclassical. The better the confinement, the more extended the neoclassical core.

In those cases where a separate analysis is possible, the ion transport in the plasma core is found to be neoclassical. Under good confinement conditions at high electron temperature, the electron core transport can also be neoclassical. With an established electric field, the highest ion and electron temperatures are measured (under different discharge conditions, however) to be 1.5 keV and 5.8 keV, respectively, as shown in Fig. 3. The presence of a radial electric field E_r reduces the heat diffusivities by up to one order of magnitude from the expected neoclassical level without such a field.

Neoclassical fluxes in stellarators depend explicitly on the radial electric field, which itself is determined by the balance of the particle fluxes. The radial electric field represents a thermodynamic force and drives the particle flux Γ ($\sim D_{11}E_r/T_e$), whereas the diffusivities (D_{11}, D_{12}) depend themselves on E_r. The nonlinear relation allows different branches of stable transport equilibria which depend operationally on T_e/T_i. The agreement between the measured radial electric field and the one computed on the basis of neoclassical transport even for turbulent plasma conditions points, as in other cases, to the intrinsic ambipolarity of

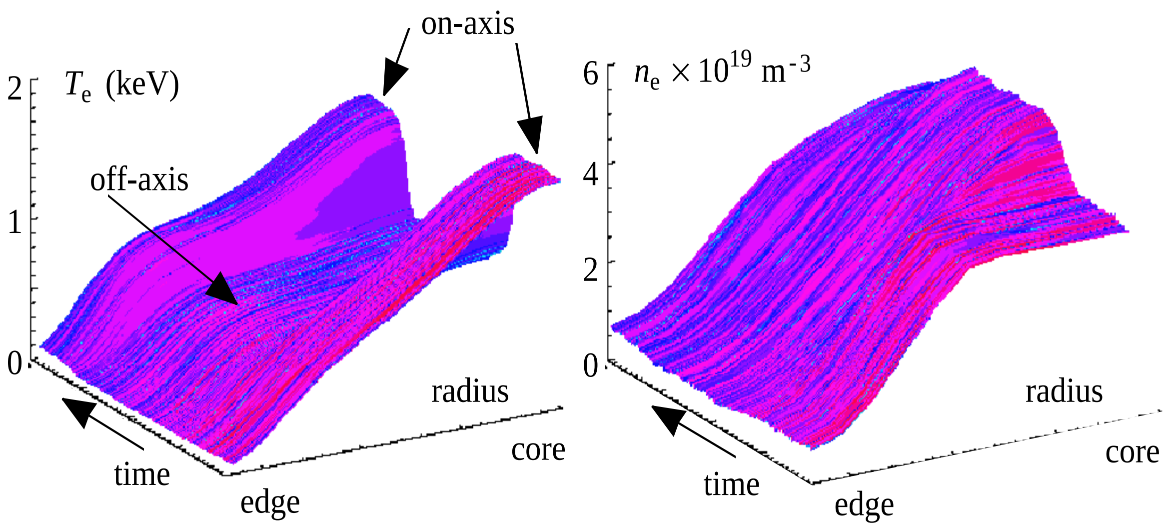

Fig. 5. The electron temperature profile, obtained from ECE (left), and the density profile obtained from a 10-channel interferometer (right), for an experimental scenario in which the ECRH power deposition was varied in steps from the core to the periphery and back again (see arrows).

the prevailing electrostatic turbulence. The highest ion temperatures are obtained with NBI when $T_e \sim T_i$. In this case the ion root develops and is characterized by a negative electric field. The highest electron temperature develops with ECRH when $T_e >> T_i$. Here the electron root is established in the plasma core, whereas the plasma periphery remains at the ion root. Detailed analysis has shown that the electron root cannot develop in W7-AS exclusively on the basis of thermal fluxes; rather the loss of nonthermal electrons energized by ECRH contributes to the ambipolarity condition.

Global confinement and improved regimes

The W7-AS energy confinement data are part of the International Stellarator Scaling ISS95 (Fig. 4). Data are selected only from the ɫ ranges around 0.334 and 0.53 where confinement is good at the L-mode level (the turbulent plasma periphery also determines τ_E in cases with neoclassical core). The τ_E scaling of W7-AS alone is $\tau_E \sim B^{0.73} \cdot P^{-0.54} n_e^{0.5} L^{2.72}$. The size scaling ($L$) is selected to have correct dimensions. It is close to the size scaling of ISS95: $L^{2.86}$.

In the above mentioned ɫ ranges, confinement can be improved above the L-mode level. Similar to the tokamak, two obviously different paths are possible: the establishment of the H-mode edge conditions and the steepening of the density profile. Apart from the insight that the H-mode is rather universal and not restricted to the conditions of tokamaks, studies on W7-AS have shown that the H-mode develops in specific ɫ ranges where poloidal flow damping (from the field structure) is low.

Particle transport

Stellarator density profiles are flat in the plasma core for central heating without central fueling. The gradients reside at the plasma edge in the range of the recycling source. With core fueling (NBI), profiles peak as a consequence of the changed source distribution. With strong central ECRH, the density profile can even become hollow. With off-axis ECRH heating and flat central temperature profiles, the core density profile peaks (see Fig. 5). EIRENE calculations show that core fueling is not dominant under the conditions of these experiments.

These observations elucidate the effects which govern the particle transport. Besides diffusion, thermal diffusion plays a role. The experimental analysis shows that the thermally driven ($\Gamma \propto T_e'$) neoclassical flux component, which is outward directed in stellarators, can explain the hollow profiles of central heating. The consequence of this term in particle transport is detrimental, because it may lead to unfavorable and even unstable density profiles in larger devices. As a consequence, the existence of a convective inward flow (by the E_r/T term or resulting from the background turbulence) superimposed onto the other two mechanisms also has an important practical aspect. This term in the transport equation was therefore carefully studied in perturbation experiments by analyzing gas oscillation and by studying the peaking of the core density profile when ECRH was switched from central to off-axis heating (see Fig. 5). The modeling of the temporal phases yields an inward velocity of about 1 m/s for the inner half, which rises towards the plasma edge to about 4 m/s. Though the particle fluxes in the core are generally close to the neoclassical level and 3-D effects of neoclassical transport cause outward-directed thermal diffusion, there remains a

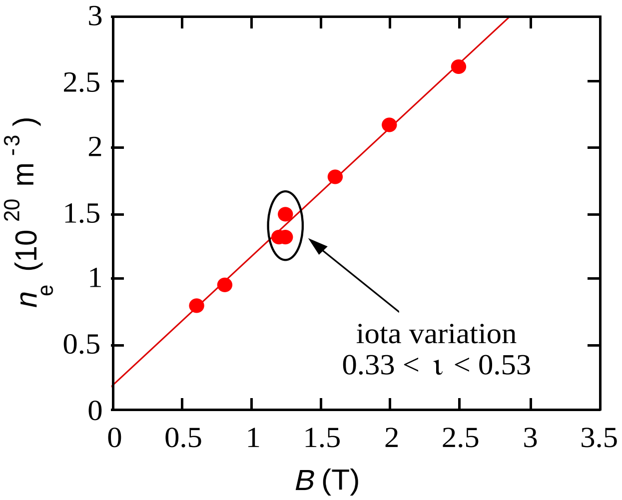

Fig. 6. Variation of the maximum operational density with magnetic field.

favorable inward flow term. Nevertheless, particle transport studies and core fueling techniques will require specific attention in large helical devices.

Impurity transport has been studied by means of different impurity injection techniques such as laser blowoff and gas oscillation. For ECRH plasmas with central electron densities of (0.4–5) × 10^{19} m^{-3}, the radiation decay time of the highest ionization states of laser blowoff injected aluminium (Al XII, Al XIII) — a measure of the global impurity confinement time — scales as $\tau_{\mathrm{Al}} \sim P_{\mathrm{ECF}}^{-0.8} n_{e0}^{1.2}$ (where P_{ECF} is the ECRH power and n_{e0} is the central electron density). The scaling is supported by local transport coefficients (diffusion coefficient D, convective velocity v) obtained from the analysis of radial and temporal soft X-ray profile developments after impurity injection. Typically for ECRH discharges, a moderate diffusion coefficient is observed in the central region ($D \sim 0.2$–1 m^2/s, decreasing with density), whereas smaller diffusion coefficients ($D \sim 0.03$–0.1 m^2/s) are obtained for the outer third of the plasma.

In plasmas with low to medium electron density (< 4 × 10^{19} m^{-3}), impurity radiation saturates and stationary conditions are achieved during the discharge pulse (typically 1 s). At higher electron densities (> 5 × 10^{19} m^{-3}), impurity radiation and Z_{eff} often do not reach a stationary state within the discharge duration but show a steady increase, with the tendency to saturate at times longer than the pulse length. Assuming constant impurity sources, this behavior is a consequence of rather low diffusion coefficients as derived from measured data, in particular in the outer region of the plasma. These discharges are also expected from modeling to reach a final intrinsic impurity concentration level related to the strength of the impurity source.

High-density operation

Stellarators can operate at high density. The density limit is caused by a breakdown of the energy balance at the plasma edge due to excessive radiation and recycling losses. The plasma decay is slow and can be influenced at any phase by a reduction of the gas flow rate or by an increase of the heating power. Of relevance for larger devices is the scaling of the maximum operating density (the value which can be stably sustained). Both edge and line-averaged density scale with power and field (Fig. 6). The edge density scaling is $n_e \sim B^{0.8} P^{0.5} L^{-0.62}$. The L scaling is selected to yield a dimensionally correct relation. With the heating power foreseen for W7-X, the operational density should surpass the one achieved in W7-AS.

The island divertor concept

W7-AS will be equipped with the first island divertor. At ɨ(a) > 0.4, the edge is bounded by a chain of intrinsic 5/m magnetic islands (with m = 8, 9, 10). The device is presently operated with poloidal inboard limiters, which will be replaced in 1999 by ten symmetrically arranged island divertor modules (designed for 5/9 boundary islands) with a strong geometrical similarity to the W7-X divertor concept. The divertor concept was prepared for by experiments on the plasma flow diversion by islands and by predictive code simulations of island divertor scenarios. A 3-D edge transport code EMC3 (Edge Monte Carlo 3-D) has been developed, coupled to the EIRENE neutral transport code, and applied to pure hydrogen plasmas (inclusion of impurity transport is under way) in the 5/9 island divertor configuration.

The results of these preliminary studies show gross agreement with tokamak X-point divertor scenarios, but in detail reflect characteristic geometrical differences. In contrast to tokamak divertors, island divertors in stellarators necessarily have a 3-D magnetic structure, toroidally discontinuous targets (localized recycling zones), smaller radial separations between target and main plasma, and, in general, longer field line connection lengths from target to target (small field line pitch inside the islands). These features affect the penetration of recycling neutrals and impurities into the main plasma, as well as the ratio of the cross-field to parallel transport (plasma flow diversion) within the SOL. Both are crucial for divertor performance. Nevertheless, the experiments mentioned give strong indications of a significant radial diversion of the plasma flow by the islands even at these conditions. With increasing density and for typical heating powers and cross-field transport coefficients, the code results predict edge parameter regimes passing through the same sequence as in tokamak divertors: from a linear SOL regime over high recycling with strong particle flux enhancement to stable (energy) detachment with strong divertor radiation and very low divertor leakage for neutrals.

Wave heating

The accessible plasma density for ECRH with electromagnetic waves in ordinary and extraordinary polarization (O- and X-mode) is limited by plasma cut-off. For the electrostatic electron Bernstein wave (EBW), the third EC mode which is able to propagate in a hot plasma, no such limit exists. However, since EBWs cannot be excited from the outside, they have to be generated via mode conversion from the electromagnetic waves. One possible way for this is the so-called OXB process. In a first step (OX process) a slow ($v_{ph} < c$) X-wave is generated at the O-mode cut-off density from a fast ($v_{ph} > c$) O-wave launched from the outside with an optimal angle oblique to the magnetic field vector. The X-wave then propagates towards the upper hybrid resonance (UHR) layer, where it is converted into an EBW (XB process). Both processes take place in the density gradient region and are very sensitive to the plasma conditions there (level of turbulence). The influence of the plasma parameters on the conversion efficiencies was investigated on W7-AS for 70-GHz ECRH. For both processes, optimal target plasma conditions could be found, so that the EBWs were generated with an efficiency of more than 80%. After the OXB process the EBWs propagate towards the dense plasma center, where they are absorbed near the cyclotron resonance layer. The radial absorption profile was estimated from the soft X-ray emission by switching the power. For our experimental plasma parameters ($T_e = 500$ eV, $n_e = 1.5 \times 10^{20}$ m^{-3}), central EBW heating could be achieved for a central magnetic field of 2.13 T. The target plasma was sustained by 360-kW NBI. Additional OXB heating with a power of 330 kW increases the plasma energy and the central plasma temperature by 30% ($\Delta W = 2.5$ kJ, $\Delta T = 110$ eV) compared with a discharge with NBI only.

Operation of ICRH from the high-field side with a narrow $k_{\|}$ spectrum showed that successful ICRF heating is possible. In resonant and nonresonant heating scenarios, the ion and electron temperatures of ECRH and NBI target plasmas were increased. Simultaneously, the plasma density could be kept constant with no rise in impurity concentration. The investigated scenarios were D(H), ^{4}He(H) minority heating (minority species in parentheses), D/H mode conversion heating, second harmonic H heating. Since recycling strongly determines the plasma composition, proper wall conditioning was imperative to obtain sufficiently low hydrogen concentration for minority heating. The efficiency of these scenarios was determined by comparing the increase in diamagnetic energy with expectations based on power scaling. Thus the efficiency was found to be comparable to that obtained in tokamaks. In particular, D(H) minority heating is similarly more efficient than second harmonic H heating. Using the same heating scenarios it was also possible to sustain target plasmas solely with ICRF. Several energy confinement times into the ICRF phase, the plasma parameters reached steady-state values of density, temperatures, and impurity radiation.

W7-AS teams
Max-Planck-Institut für Plasmaphysik
EURATOM Association
Garching, Germany

E-mail: fritz.wagner@ipp-garching.mpg.de

The dependence of confinement on rotational transform and magnetic shear in Wendelstein 7-AS

Magnetic shear is an important design parameter for helical devices, entering for example into basic criteria for MHD stability, microinstabilities, and flux surface quality. Wendelstein stellarators have low global shear in the vacuum field and provide MHD stability by a global magnetic well. Major resonances can be excluded from the confinement volume by proper choice of the rotational transform. Thus high flux surface quality is obtained. At finite β, magnetic shear may increase to moderate values because of the pressure-driven bootstrap current and Pfirsch-Schlüter (PS) currents which in W7-AS are reduced but still significant. Optionally, shear can be modified by externally (e.g., inductively) driven currents created by electron cyclotron (EC) or neutral beam (NB) heating (Fig. 1).

With moderate shear, which is typical for the standard mode of net current-free operation, confinement in Wendelstein stellarators exhibits a strong dependence on the boundary value $\iota(a)$ of the rotational transform with pronounced maxima in narrow operation windows around the low-order rational values 1/2, 1/3, ... [1, 2]. An example from ECRH discharges in W7-AS is given in Fig. 2. At the confinement optima the electron temperature profile, $T_e(r)$, has steep gradients throughout the plasma volume but is flat in the outer half for the degraded situations. The centrally flat density profile, $n_e(r)$, is rather robust (enhanced particle losses are replaced by feedback-controlled gas injection). Furthermore, when sufficient shear is introduced in W7-AS by an inductive plasma current, the strong dependence on $\iota(a)$ is lost and confinement

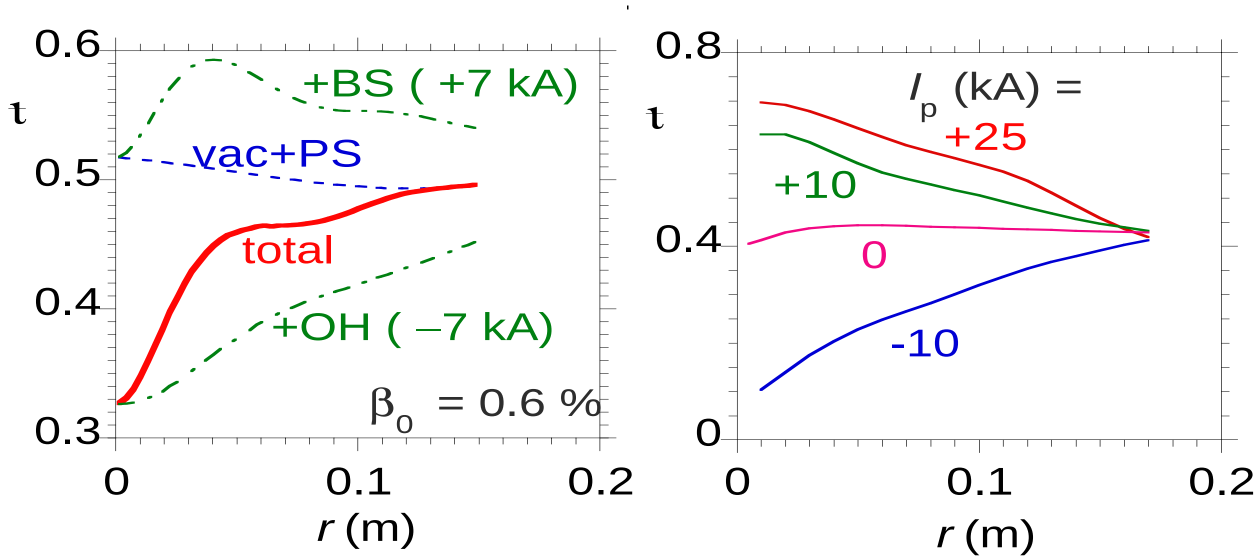

Fig. 1. ι profiles in W7-AS with inductive current control. Left: contributions to ι for $I_p = 0$. Right: total ι at different net currents. Plasma conditions: $B = 2.5$ T, $P = 450$ kW, $n_e \sim 4 \times 10^{19}$ m^{-3}.

improves to the optimum level for any $\iota(a)$ (Fig. 3). With high shear (25-kA case) the electron heat conductivity is reduced to the neoclassical level up to radii $r/a \sim 0.7$ [4]. This is independent of the sign of shear. All discharges under consideration have moderate β ($\beta_0 \leq 0.6\%$) and are dominated by electron transport ($T_e = 2$ keV, $T_i = 0.4$ keV).

It is unlikely that these dependencies can be explained by island formation due to the static perturbations of the vacuum field ("natural" $5/m$ components from the 5-fold toroidal periodicity, 1/2 and 1/3 components from field errors) which are quantitatively known from flux surface mapping [3]. Rather, it is suggested that internal perturbations at higher order rational surfaces arising from MHD instabilities or plasma turbulence enhance the anomalous electron energy transport when magnetic shear is low in the presence of such rational ι values, and that these perturbations are suppressed by magnetic shear. As discussed in Refs. [1] and [2], the narrow ι ranges for optimum confinement are generally characterized by the absence of the otherwise densely spaced higher order rational ι values.

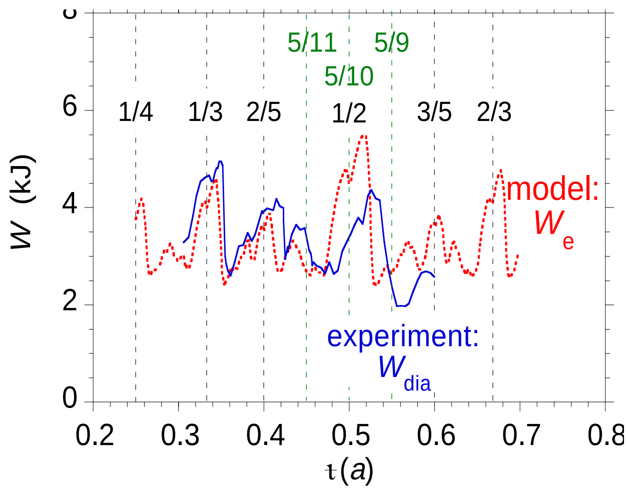

Fig. 2. Plasma energy (experiment) and electron kinetic energy (model) vs boundary value of the total rotational transform, $\iota(a)$, for $I_p = 0$. ($B = 2.5$ T, $P = 340$ kW, $n_e \sim 2.5 \times 10^{19}$ m^{-3}.)

The experimental findings suggest a simple empirical ansatz for the electron heat conductivity χ_e [5]:

$$\chi_e\,(r, \iota, \iota') = \chi_0(r) + \Sigma\, \chi_{nm}\,(\iota, \iota'),$$

$$\chi_{nm} = \alpha_{nm} \exp\,(-\,|\iota - n/m|/\delta - \gamma\,|\iota'|).$$

χ_0 accounts for the transport in the absence of resonances; that is, at optimum confinement. It includes the neoclassical contribution to χ_e. χ_{nm} describes an additional enhancement of χ_e near a rational value $\iota = n/m$, which is damped with increasing absolute value of the magnetic shear $\iota' = d\iota/dr$. The amplitudes α_{nm}, the width δ of the perturbed region, and the damping constant γ have to be determined by experiments which vary $\iota(r)$ and $\iota'(r)$.

Rotational transform, magnetic shear (from bootstrap and inductive current), and confinement are self-consistently coupled by using $\chi_e\,(r, \iota, \iota')$ in the electron power balance to calculate $T_e(r)$, which in turn basically determines the toroidal bootstrap and inductive current densities, j_{BS} and j_{OH}, and thus the ι profile. The solution is obtained by iteration. The bootstrap current density is approximated by $j_{BS} = 0.7 j_{BS}^{HH}$, with the bootstrap current density j_{BS}^{HH} in a circular tokamak [6]. The factor 0.7 adjusts the current to the value obtained with the DKES code for optimum confinement. For the modeling of discharges with inductive net current control, the inductive current density profile is calculated from the tokamak neoclassical conductivity [6]

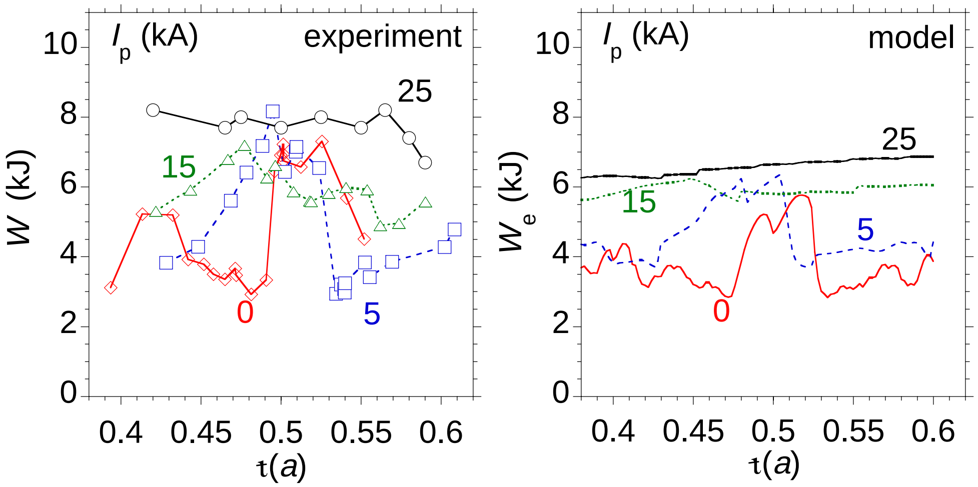

Fig. 3. Plasma energy (experiment) and electron kinetic energy (model) vs ɫ(a) for various net plasma currents I_p. ($B = 2.5$ T, $P = 450$ kW, $n_e \sim 4 \times 10^{19}\ \mathrm{m^{-3}}$.)

and normalized such that bootstrap and inductive current add up to the given net plasma current I_p. The PS current is neglected. Density and power deposition profiles, boundary value of the rotational transform, and, optionally, a net plasma current are input to the model.

In the calculations, rational values up to $m = 20$, $\delta = 0.004$, $\gamma = 1.1$ m, $\alpha_{nm} = 1.1 g_{nm}^{-1}\ \mathrm{m^2/s}$, $Z_{\mathrm{eff}} = 2$, and $T_e(a) =$ 100 eV have been used. g_{nm} is the degeneracy of an n/m value; that is, every rational number is counted only once. The results are compared in Figs. 2 and 3 with the experiment. The experiments of Fig. 2 were conducted with maximum aperture of the top/bottom limiters, i.e. for ɫ(a) > 0.4 the radius of the last closed surface shrinks due to separatrix formation by the $5/m$ "natural" islands. This is not accounted for in the calculation, which partly explains the deviation between experiment and model at large ɫ(a). In the case of Fig. 3 the limiter aperture was strongly reduced to weaken the influence of the "natural" islands. The model qualitatively reproduces the basic dependences of confinement on the experimental control parameters, ɫ(a) and I_p, supporting the hypothesis of the impact of rational ɫ values on confinement.

If in the model the constraint of a fixed net plasma current is relaxed (no inductive current control, $I_p = I_{BS}$) two branches of solutions with high or low confinement are predicted, depending on the starting point of the iteration (Fig. 4). On the high confinement branch, the bootstrap current is sufficiently high to lift the total ɫ from the vacuum field profile upwards into the next resonance-free region. On the low confinement branch, the bootstrap current is too small. This bifurcation has not yet been studied experimentally.

R. Brakel and the W7-AS Team
Max-Planck-Institut für Plasmaphysik
EURATOM Association
D-85748 Garching, Germany
E-mail: brakel@ipp.mpg.de

References

[1] G. Grieger, H. Renner, and H. Wobig, *Nucl. Fusion* **25,** 1231 (1985).

[2] H. Wobig et al., *Plasma Phys. Controlled Nucl. Fusion Research (Proc. 11th Int. Conf. Kyoto, 1986)* Vol. 2 (IAEA, Vienna) 369 (1987).

[3] R. Jänicke et al., *Nucl. Fusion*, **33,** 687 (1993).

[4] R. Brakel et al., *Plasma Phys. Controlled Fusion* **39B,** 273 (1997).

[5] R. Brakel et al., *Proc. 25th EPS Conf., Prague* (1998), p. 423.

[6] F. L. Hinton and R. D. Hazeltine, *Rev. Mod. Phys.* **48,** 239 (1976).

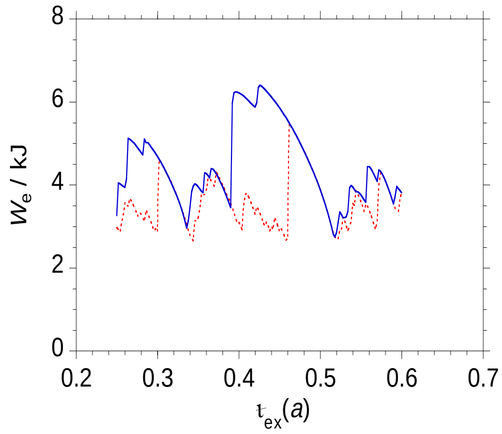

Fig. 4. The two branches of solutions without net current control. $ɫ_{ex}$(a) is the boundary value of the external rotational transform. (Conditions of Fig. 2.)

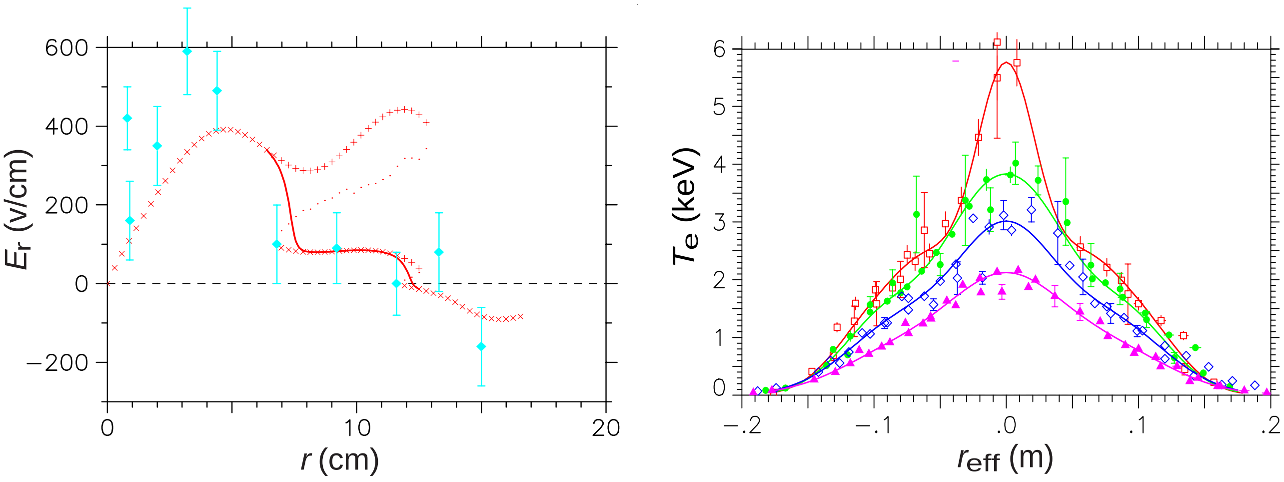

Fig. 1. Left: E_r profile obtained with electron root conditions in the plasma center (full diamonds: CXRS, DKES code calculations with crosses for stable roots and small dots for unstable roots). Right: Electron temperature profiles from an ECRH power scan with P_{ECRH} = 200 kW, 400 kW, 800 kW, 1200kW. The electron root $E_r > 0$ develops with $P_{ECRH} \geq 400$ kW, resulting in a strong increase of central T_e.

Bifurcations of neoclassical and turbulent transport in W7-AS

Confinement bifurcations are observed in W7-AS plasmas in both neoclassical and turbulent transport regimes. The maximum values of T_e, T_i, and τ_E obtained are achieved after a transition to one of the improved confinement states. An important element of the observed bifurcation processes is the radial electric field, E_r.

In general, the dependence of the radial particle fluxes on E_r is nonlinear and multiple solutions (referred to as "roots") for the ambipolarity condition of the particle fluxes may exist. Under most plasma conditions, the ambipolarity of the particle fluxes is fulfilled in the ion root with a negative E_r and $T_i \leq T_e$. For sufficiently high temperatures in the central part of the plasma the neoclassical level of transport is reached. In general the measured values of E_r agree with those computed on the basis of ambipolar neoclassical fluxes even for radii where the experimental fluxes exceed the predictions of neoclassical theory [1]. This indicates that the anomalous particle fluxes involved are ambipolar.

Three types of confinement bifurcations will be summarized in the following: (1) A bifurcation between the ion root and the electron root of the ambipolarity condition is observed with the electrons in the very long mean free path and $T_i << T_e$ in the very center of the plasma. The electron root is characterized by a strongly positive E_r and thus reduced electron fluxes. (2) At the plasma boundary, (i.e., under ion root conditions $E_r < 0$ and $T_i \leq T_e$), the transition to the H-mode occurs as a fast reduction of turbulence and transport associated with a decrease of E_r towards more negative values. As a consequence, broad density and temperature profiles with maximum gradients a few centimeters inside the confinement region occur. (3) Optimum confinement in W7-AS is observed if, under ion root conditions, the plasma undergoes a slow transition (i.e., on a time scale of a few confinement times) to broad profiles for T_i and T_e but with a narrow, peaked density profile. A strong negative E_r develops in the region of the density gradient.

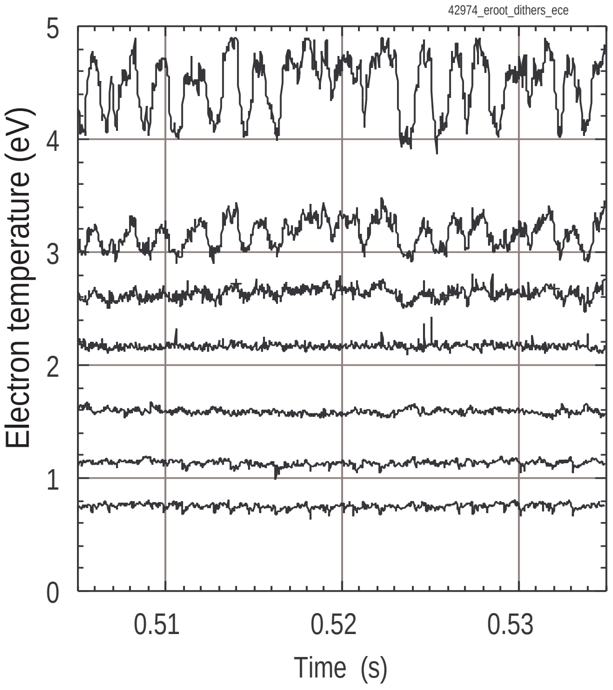

Fig. 2. Time traces of electron cyclotron emission (ECE) displaying a dithering electron root feature in the plasma center.

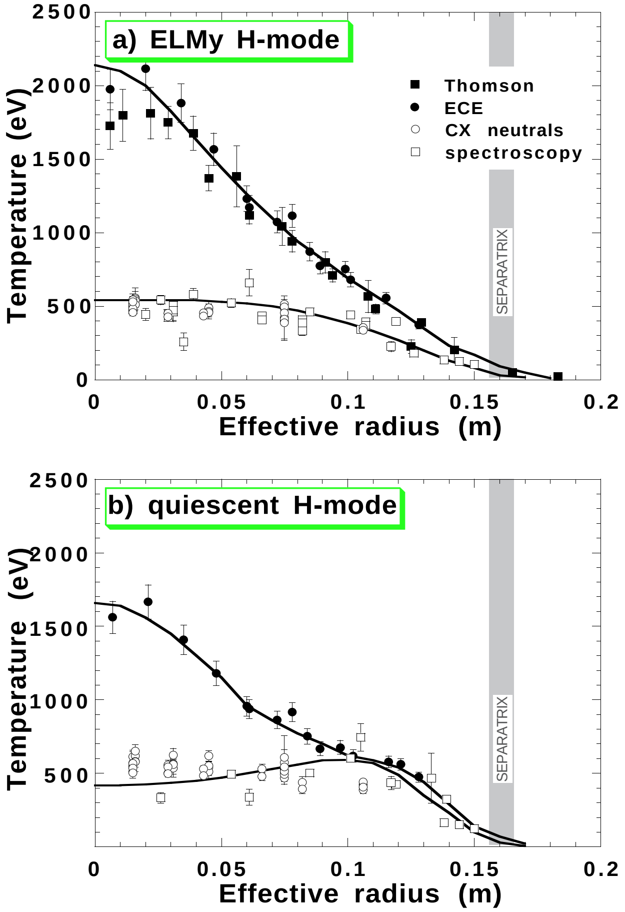

Fig. 3. Temperature in an ECR-heated discharge during the quiescent H-mode (b) and in the ELMy state prior to the transition (a). T_e is obtained from Thomson scattering and ECE, T_i from CX neutrals, active CXRS, and passive B IV emission. The quiescent H-mode is achieved by a 20% increase of the density; thus the central electron temperature decreases with respect to the ELMy prephase.

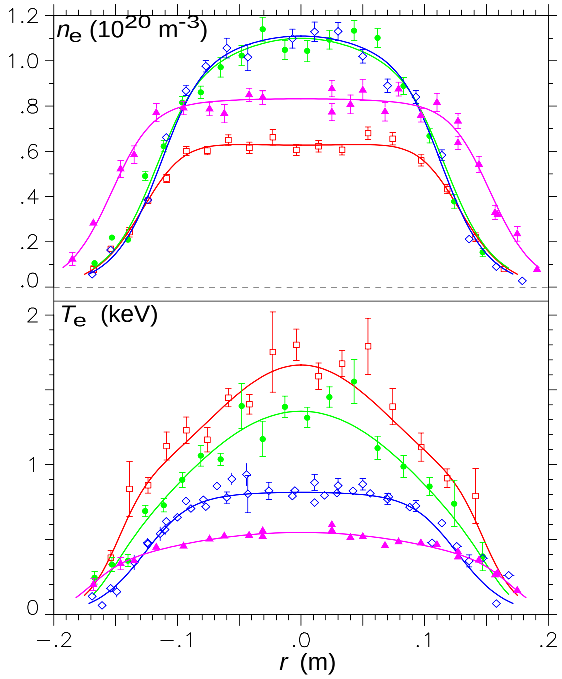

Fig. 4. Profiles of (a) electron density and (b) electron temperature for optimum confinement discharges at different density and heating conditions: red line/open squares: NBI (1350 kW) + ECRH (750 kW), green lin /filled circles: NBI (1300kW) + ECRH (350 kW), blue line / open diamonds: pure NBI (450 kW). A discharge with degraded confinement is given as reference by a magenta line/filled triangles: pure NBI (850 kW).

Transition from ion root to electron root

With the electrons in the very long mean free path [heated by electron cyclotron resonant heating (ECRH) up to T_e = 6 keV, see also V. Erckmann and H. Maaßberg, "Recent results for ECRH and ECCD on the W7-AS Stellarator," in this issue], the electron root is accessible in the plasma center of W7-AS [2]. The region with a strongly positive E_r [Fig. 1(a)] is related to an additional peaking of the central T_e profile indicating improved electron energy confinement [Fig. 1(b)], whereas the profiles of T_i and n_e remain flat. The experimental χ_e is more than an order of magnitude lower than the neoclassical value if E_r is not taken into account. For the transition to the electron root, power and density thresholds which depend on the specific magnetic configuration have been found [Fig. 1(b)]. In particular the electron root feature is achieved with lower ECRH power P_{ECRH} and at even higher densities if a significant fraction of trapped particles exists. Therefore, it is concluded that suprathermal electrons trapped in the toroidal mirror of the ECRH launching plane are responsible for an additional electron flux which has to be included in the ambipolarity condition [3].

The dynamic behavior of the electron root feature supports this picture: If P_{ECRH} is decreased below the threshold power, the central peak of the T_e profile decays much faster than the intermediate part of the profile, which is determined by the ion root [4]. If the nonlocal (convective) radial flux of ripple-trapped suprathermal electrons contributes significantly to the ambipolarity condition, thus driving the electron root feature, the strongly positive E_r should decay on the ∇B-drift scale (several tens of microseconds). Then the neoclassical diffusivity decreases nearly instantaneously to the ion root level. A dithering between the electron and the ion root can be observed if the ECRH power density is close to the threshold (Fig. 2). These findings are very similar to the observations of fast spontaneous transitions of the electrostatic potential observed in CHS [5].

Transition to the H-mode

This transition occurs as the establishment of an edge transport barrier with the characteristics well known from other devices: The gradients of n_e, T_e, and T_i profiles

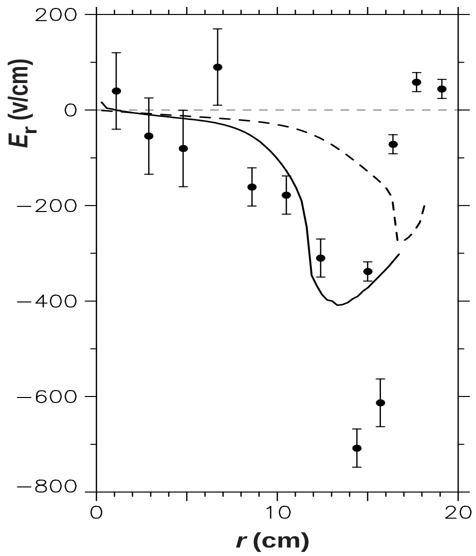

Fig. 5. Radial electric field measured by CXRS (solid circles) in comparison with the neoclassical prediction (solid line) for the optimum confinement discharge marked with a solid line in Fig.4. A dashed line gives the neoclassical prediction for the degraded confinement (Fig. 4, dashed line) for comparison.

steepen in a layer extending over the first 3–4 cm inside the separatrix (Fig. 3) [6]. Fluctuations of edge density and magnetic field are reduced by about an order of magnitude, and the value of the negative radial electric field increases [7]. A strongly peaked radiation profile develops in the H-mode and leads to a degradation of the edge temperature pedestal after a few confinement times. The quiescent H-mode requires a threshold density and occurs for well-defined magnetic edge topologies only when poloidal flow damping from the magnetic field structure is low [8].

In every case the quiescent edge-localized mode (ELM)-free H-mode is preceded by a phase characterized by quasiperiodic ELMs and an energy confinement and profiles close to the stationary turbulent state. The ELMy state can be maintained over the whole discharge with plasma parameters controlled to be close to the threshold. Each ELM occurs as a burst of turbulence associated with a transport event which directly affects only the outer part of the confinement region. The transition to the H-mode itself, that is, the increase of the gradients, can be defined by the disappearance of the ELMs. As plasma parameters become more different from the those at the quiescent H-mode transition, the single ELMs become less pronounced, and their repetition rate increases and tends to be less regular. No such clear transition from a state with the plasma edge characterized by ELM-like transport events and a stationary turbulent “L-mode” is found [9].

Transition to optimum confinement

Optimum confinement in W7-AS is observed after the plasma undergoes a slow transition (on a confinement time scale) to a state with a peaked density profile and a small edge density while $\langle n \rangle$ remains constant. Broad temperature profiles with $T_i \cong T_e$ at the plasma edge develop. The steep outer temperature gradients allow for temperatures high enough that for $r < 0.7a$ the experimental particle and heat fluxes are on the level of neoclassical transport with its strongly rising temperature characteristic [4,10]. A very strong negative radial electric field $E_r \leq 700$ V/cm develops in the region of the density gradient [1]. It follows the expectations from the ambipolarity condition in the ion root where

$$E_r \propto T_i(\nabla n/n) + (D_{21}/D_{11})\nabla T_i\ ,$$

with D_{21}, D_{11} being the diagonal and off-diagonal matrix elements of the ion transport matrix. Thus a large E_r is expected for strong ∇T_i at the edge, and for a density gradient that extends inward in a region where, because of the broad temperature profile, T_i is large. Close to the plasma boundary where neoclassical theory fails, the observed values of E_r can be even stronger than the ambipolar neoclassical prediction [1].

The operational conditions required for a transition to the optimum confinement regime are a threshold NBI heating power and low recycling. If the NBI heating power only marginally exceeds the threshold, the transition to optimum confinement is delayed [10]. Low recycling is mandatory for access to this regime and also helps to maintain density control after optimum confinement is reached. The central particle fueling by NBI is beneficial to achieving profile peaking. With this regime, energy confinement up to a factor of two above the W7-AS data of the ISS95 scaling has been found. For low NBI heating power (absorbed power 350 kW, $\langle n \rangle \sim 10^{20}$ m^{-3}) the maximum energy confinement time measured in W7-AS, $\tau_E = 55$ ms, was achieved [10]. Maximum ion temperatures $T_i = 1.5$ kV are obtained for discharges with the same characteristics but at lower densities, $\langle n \rangle \sim 0.5 \times 10^{20}$ m^{-3} and higher heating power ($P_{\mathrm{abs}}^{\mathrm{NBI}} = 850$ kW + 350 kW ECRH) [11].

The strong outer temperature gradients indicate a reduced anomalous transport at the plasma boundary. It is speculated that the $\boldsymbol{E} \times \boldsymbol{B}$ flow shear there reduces the energy and particle fluxes carried by turbulence. In the optimum confinement state, the level of density and magnetic fluctuations at the plasma edge is generally reduced by about a factor of two (in contrast, at the onset of the quiescent H-mode an order of magnitude reduction is observed). At the transition to the optimum confinement regime, fluctuations do not change abruptly as at the onset of the quiescent H-mode but decrease along the time scales of the profile changes. Simultaneously, the coherence time of quasiturbulent and coherent mode activity decreases, possibly indicating the effect of shear flow decorrelation. The merit of the optimum confinement state thus would be to allow for a strong ambipolar E_r driven by broad temperature profiles and a peaked density profile where the latter is achieved by low recycling. In turn the resulting strong negative E_r reduces ion fluxes and the corresponding $\boldsymbol{E} \times \boldsymbol{B}$ shear at the plasma edge leads to reduced anomalous transport, thus closing the loop by allowing for strong temperature gradients.

Discharges within the operational range of the quiescent H-mode, but with heating and recycling conditions required for optimum confinement, show that the H-mode with its broad density profile develops first and temporarily hinders a transition to optimum confinement. The strong increase of central radiation degrades the edge temperature pedestal of the quiescent H-mode. Simultaneously, the density profile starts to become narrower, accompanied by a series of large ELMs which help to reduce the edge density [4]. During optimum confinement, ELM-like transport events with irregular repetition rate are observed, in contrast to operation close to the threshold of the quiescent H-mode, they affect a layer extending deeper in the plasma [9].

M. Hirsch, M. Kick, H. Maaßberg, and U. Stroth for the W7-AS Team
Max-Planck-Institut für Plasmaphysik
EURATOM Association
Garching, Germany

References

[1] J. Baldzuhn, M. Kick, and H. Maaßberg, Plasma Phys. Controlled Fusion **40** (1998) 967.

[2] H. Maaßberg, C. D. Beidler, K. S. Dyablin, U. Gaspari-no, S. Murakami, submitted to Plasma Phys. Controlled Fusion *(*1998).

[3] S. Murakami et al., Proc. 17th IAEA Conf. (Yokohama, 1998), IAEA-CN-69 / TH 2/1.

[4] M. Kick et al., Proc. 25th EPS Conf. (Prague) (1998).

[5] A. Fujisawa et al., Plasma Phys. Controlled Fusion **40** (1998) 627.

[6] M. Hirsch et al., Plasma Phys. Controlled Fusion **40** (1998) 631.

[7] F. Wagner et al., Plasma Phys. Controlled Fusion, **36** (1994) A61.

[8] H. Wobig and J. Kisslinger, Proc. 24th EPS Conf. (Berchdesgaden) *(*1997*)*.

[9] M. Hirsch et al., Proc. *25th EPS Conf. (Prague)*, **22C** (1998) 2322.

[10] U. Stroth et al., Plasma Phys. Controlled Fusion **40** (1998) 1551.

[11] M. Kick et al., in *Proc. 16th IAEA Conf. (Montreal, 1996)* (IAEA, Vienna, 1997) Vol. 2, p. 27.

Polarimetric line density measurements on W7-AS using the Cotton-Mouton effect

Polarimetry makes use of the birefringence of a magnetized plasma. In the past, it was used to determine current profiles in tokamaks. A new application has been studied in the last few years: the robust measurement of the line integrated density, which is of special importance for long-pulse operation as expected for future devices like the W7-X stellarator or for ITER. In this context a Cotton-Mouton polarimeter was proposed for ITER [1].

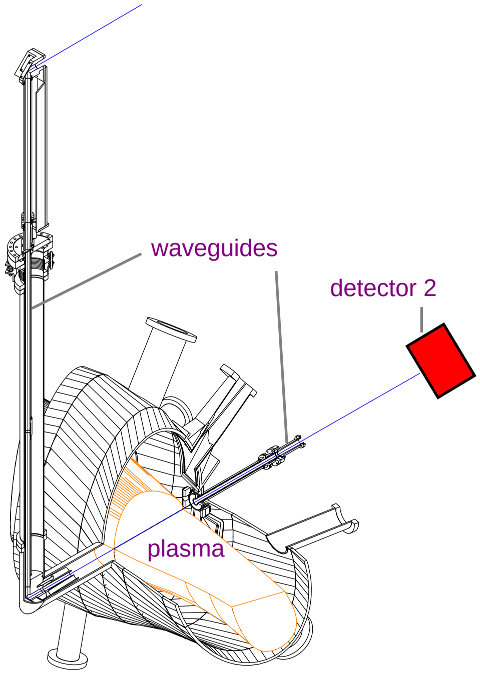

Fig. 1. Beam path at the W7-AS stellarator.

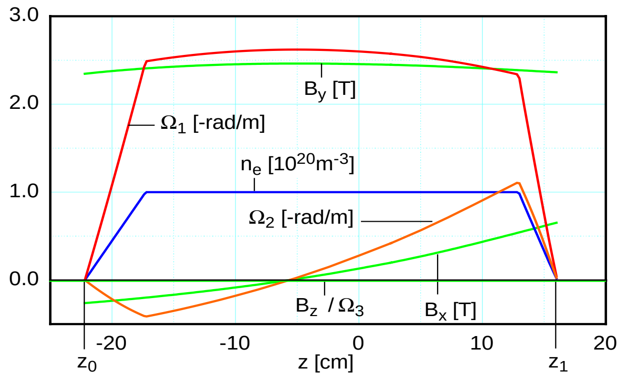

Fig. 2. Plasma parameters along the line of sight for a typical configuration of the magnetic field in W7-AS.

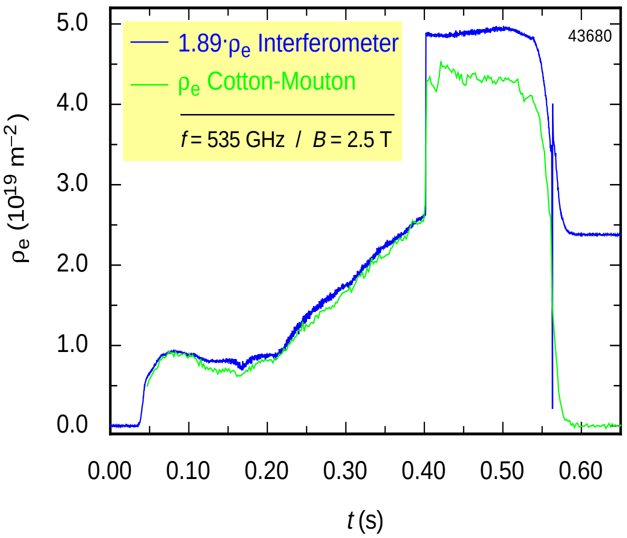

Fig. 3. Plasma discharge with pellet injection. The interferometer shows fringe jumps, while the Cotton-Mouton polarimeter remains stable.

Both the Faraday and the Cotton-Mouton magneto-optic effects can be used for measurements of the line density. The Faraday effect is caused by circular birefringence, which leads to a phase shift between the left- and the right-handed circularly polarized waves, resulting in a rotation of the plane of polarization; the magnetic field is parallel to the direction of propagation.

The Cotton-Mouton effect is observed if the magnetic field is perpendicular to the direction of propagation. The characteristic waves are linear polarized waves with the plane of polarization parallel (O-mode) and perpendicular (X-mode) to the magnetic field. The phase difference caused by linear birefringence leads to a change of the wave ellipticity. If the magnetic field ***B*** along the line of sight is known, the line density can be determined by a measurement of this phase difference.

Optimal conditions are provided by the Wendelstein stellarators, which offer lines of sight where |***B***| is almost constant and the field component $B_{||}$ in the propagation direction of the wave is negligible. In this case the position of the plasma and the density profile need not be known and the influence of the Faraday effect is negligibly small.

Calculation of changes in the polarization state

Owing to the small twist of the magnetic field, it is not possible to obtain pure O- and X-modes along the whole line of sight. In addition, a possible misalignment leads to $B_{||} \neq 0$ (but still small), which provokes an unwanted Faraday effect. A general formalism [2,3] is used to describe the changes of the polarization state along the probing beam path. The polarization state is described by the three Stokes parameters s_1, s_2, and s_3, the components of the Stokes vector **s**. The evolution along the line of sight (z-direction) is $d\mathbf{s}(z)/dz = \vec{\Omega}(z) \times \mathbf{s}(z)$. The vector $\vec{\Omega}(z)$ describes the plasma-wave interaction. The components Ω_1 and Ω_2 of the vector $\vec{\Omega}(z)$ represent the Cotton-Mouton effect, while Ω_3 describes the Faraday effect. The quantity Ω_2 is non-zero owing to the twist of the magnetic field. The beam path as shown in Fig. 1 and an example of n_e, ***B***, and the components of $\vec{\Omega}$ along the chosen line of sight in W7-AS is shown in Fig. 2.

In the case of a dominating Cotton-Mouton effect and sufficiently small twist of the magnetic field, $\Omega_1 \gg \Omega_2, \Omega_3$, the phase shift between the x- and the y-components of a launched wave with the direction of the magnetic field being mainly in the y-direction is given by the quantity

$$W_1 = \int_{z_0}^{z_1} dz\,\Omega_1(z) .$$

For $\omega^2 \gg \omega_p^2$ and $\omega^2 \gg \omega_c^2$, where ω_p and ω_c are the plasma and electron cyclotron angular frequencies and $\omega = 2\pi f$ is the probing beam frequency, the approximation $\Omega_1 = [e^2/(2cm^2\omega^3)] \cdot \omega_p^2(B_x^2 - B_y^2)$ can be made. In this approximation, the quantity W_1 is exactly proportional to the electron line density

$$\rho_e = \int_{z_0}^{z_1} n_e(z)dz .$$

In the case of an almost constant magnetic field B, W_1 becomes independent of the shape of the density profile. A more extensive discussion is given in Refs. [4–6].

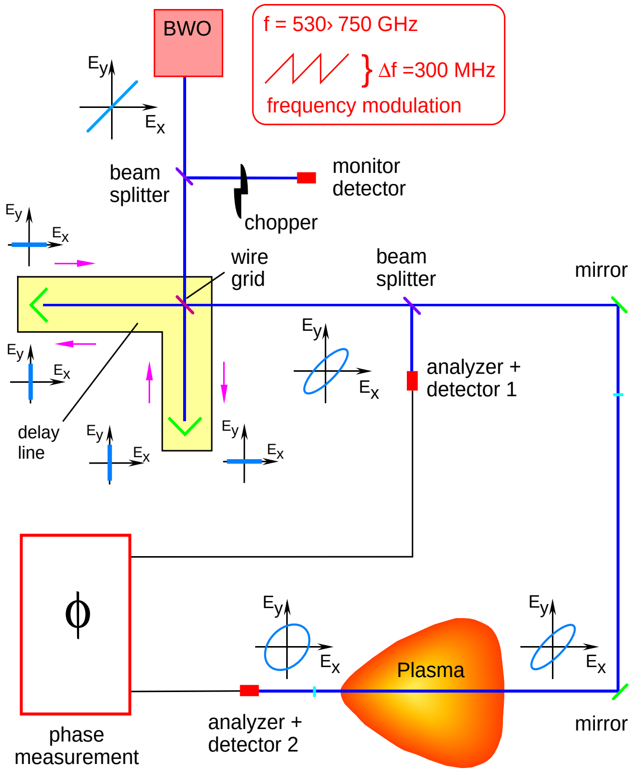

Fig. 4. Experimental set-up at the W7-AS stellarator.

Measurement of the Cotton-Mouton effect

The quantity W_1 contains the line density ρ_e. Knowledge of B allows the dependence of W_1 on ρ_e to be determined. To measure W_1, a modulation technique as proposed in Ref. [3] is used. The probing wave is composed of two orthogonally linearly polarized waves. The phase between these waves is linearly shifted with a modulation frequency ω_m, leading to an elliptical modulation of the probing wave. The Stokes parameters before the wave enters the plasma are $s_1(z_0) = 0$, $s_2(z_0) = \cos(\omega_m t)$, and $s_3(z_0) = \sin(\omega_m t)$, assuming identical intensity of the probing wave components.

The Stokes parameter $s_2(z_1)$ after the waves pass through the plasma becomes $s_2(z_1) = \cos(\omega_m t + W_1)$ (see Refs. [4–6]). In this way, W_1 is just the phase difference between the Stokes parameters $s_2(z_0)$ and $s_2(z_1)$.

The expression for Ω_1 given above is valid for high frequencies, but can lead to errors up to about 10% for the set-up at W7-AS. Therefore more exact calculations are made using an expression for Ω_1 from Ref. [2] to obtain the line density ρ_e [4, 5]. An example for a measurement of ρ_e is shown in Fig. 3. By performing systematic scans of the magnetic field at two different frequencies (535 and 627 GHz) and comparing the measured phase differences with calculated values, it could be verified that the Faraday effect, which depends on $\omega^{-2}B_{\|}$, is negligible. More results are discussed in Refs. [4, 5].

Experimental set-up

The total experimental set-up is sketched in Fig. 4. A backward wave oscillator (BWO) is used as a tunable radiation source in the frequency range 500–650 GHz. Oversized waveguides of 24 mm diameter are used throughout in the guided wave sections. The modulation of the wave ellipticity is accomplished as described in Ref. [7]. A polarizing wire grid reflects the *y*-polarized component of the wave, whereas the *x*-component is guided to a delay line. After reflection at two mirrors which rotate the polarization plane by 90°, this component is added to the reflected one. The phase difference of the two components depends on the wave frequency and the length of the delay line. A BWO-frequency modulation with $\omega_m/2\pi = 47$ kHz and $\Delta f = 300$ MHz then transforms to an ellipticity modulation of the probing wave. Detectors 1 (reference detector) and 2 (signal detector) with 45° analyzers deliver signals proportional to $s_2(z_0)$ and $s_2(z_1)$, respectively. Their phase difference is the quantity of interest, which is evaluated digitally. For a typical configuration with $B = 2.5$ T, the phase difference is 15° for a line density of $10^{19}\ \mathrm{m}^{-2}$.

Small changes of polarization in the transmission line cause errors of about 1% in the W_1 measurement. Considering also misalignments in the probing beam path, numerical calculations result in maximum errors between –3% and +2% for the lowest magnetic field (1.25 T) where the effect is smallest. Another error results from different phase shifts for the *x*- and *y*-components in the transmission line in combination with BWO instabilities, which lead to phase errors of about 1°. Other errors include amplitude modulation caused by the frequency-dependent vacuum window transmission, plasma diamagnetism, and uncertainties in the probing beam frequency. Errors owing to refraction effects, which could lead to a path length difference for the *x*- and the *y*-polarized components of the probing beam, are negligible as proven by ray tracing calculations. The relative errors sum up to an error range of –5.5% to 5.6% for $B = 1.25$ T and –4.5% to 5.1% for $B = 2.5$ T at the maximum, including maximum misalignment of the probing beam. More information about the experimental set-up and error sources is given in Ref. [4].

Conclusion

The capability of the Cotton-Mouton effect to provide a robust measurement of the line integrated density at W7-AS has been demonstrated. An optimized set-up is proposed for W7-X. Both W7-X and W7-AS offer a favorable magnetic field topology for the method.

The main problems of the W7-AS set-up are the transmission properties of the oversized waveguides with respect to conservation of the polarization state; this is not discussed here. Changes in the polarization state could be avoided in an advanced experimental set-up by using quasioptical transmission techniques if space allows.

Ch. Fuchs and H. J. Hartfuss
Max-Planck-Institut für Plasmaphysik
EURATOM Association
D-85748 Garching, Germany

References

[1] P. Buratti, proposed and discussed at meetings with the European Home Team on microwave diagnostics for ITER.

[2] S. E. Segre, Plasma Phys. **20**, 295 (1978).

[3] S. E. Segre, Phys. Plasmas **2**, 2908 (1995).

[4] Ch. Fuchs, Messung des Cotton-Mouton-Effekts am Stellarator W7-AS, Ph.D. thesis, Universität Regensburg, 1998.

[5] Ch. Fuchs and H. J. Hartfuß, Phys. Rev. Lett. **81**, 1626 (1998).

[6] Ch. Fuchs and H. J. Hartfuß, Rev. Sci. Instrum., to be published in January 1999.

[7] V. F. Shevchenko, A. A. Petrov, V. G. Petrov, and Y. A. Chaplygin, Plasma Phys. Rep. **22**, 28 (1996).

Recent results with ECRH and ECCD on the W7-AS stellarator

Investigations on electron cyclotron resonance heating (ECRH) and electron cyclotron current drive (ECCD) at W7-AS [1] were continued with an upgraded ECRH power of up to 1.3 MW at 140 GHz, which corresponds to a resonant magnetic field of 2.5 T at second harmonic X-mode (X2). The heating experiments cover the full accessible density range up to the cut-off density of 1.25×10^{20} m^{-3}, whereas we have restricted the ECCD experiments to densities around 0.25×10^{20} m^{-3}. The microwaves are absorbed in a narrow region around the resonant magnetic field, and thus the power density increases up to 50 MW/m^{3} in a flux surface average, which is far beyond the limits where linear theory holds and nonlinear phenomena are expected to occur. At high power density, the electron distribution function flattens at the resonance and the absorption is shifted towards higher energies, thus generating a suprathermal tail [1,2]. This quasilinear effect increases the ECCD efficiency with respect to linear theory. Nonlinear wave-particle interaction, which is maximum for ripple-trapped electrons with small parallel velocities, is, however, expected to reduce the ECCD efficiency. Furthermore, a strong deformation of the electron distribution function may be unstable, thus affecting the driven current.

Central confinement with strong ECRH

Experiments with strong X2-mode heating were performed in a wide density range at constant input power of 1.3 MW in low-field-side launch in the equatorial plane. Radial profiles of T_e and n_e are shown in Fig. 1. The central electron temperatures range from 5.7 keV at 1.7×10^{19} m^{-3} to 3 keV at 7.5×10^{19} m^{-3}. A pronounced steepening of the temperature gradients is seen in the center of the plasma at densities below 4×10^{20} m^{-3}. The stationary transport analysis of these discharges results in a central ($r/a < 0.3$) electron heat diffusivity that is well below the neoclassical heat diffusivity, once electric fields are neglected. Strong positive radial electric fields up to 50 kV/m were measured in the plasma center, which lead to good agreement with neoclassical theory including electric fields ("electron root solution"). It is worth noting that the ions are energetically decoupled from the electrons under these conditions and the energy balance is dominated by the electrons.

The appearance of the electric fields — and the corresponding steep temperature gradients — shows a threshold behavior at a density around $(0.2–0.4) \times 10^{20}$ m^{-3}. Similar behavior was measured during a power scan from 0.2 MW to 1.3 MW input power at a constant density of 0.2×10^{20} m^{-3}, where the steepening occurred between 0.2 and 0.4 MW. The discharge could be placed at the threshold by careful adjustment of the heating power density while tuning the deposition region. The central electron temperature then jumps iteratively between two states of low (e.g., 4-keV) and high (5-keV) temperature during one discharge with some hysteresis between rise-time and fall-time constants. These experiments are explained by a substantial loss of fast trapped particles driven by ECRH itself, which in turn generates a positive electric field with its beneficial effect on the bulk electrons [3,4]. This picture is consistent with the results of switching experiments, where the central confinement is lost on a fast time scale (< 0.3 ms), whereas the remaining profile relaxes on the diffusion time scale. Also, these switching experiments display a threshold nature while switching from 1.2 to 0.8 to 0.4 MW.

Electron cyclotron current drive

A toroidal launch angle scan was performed at 1.2 MW of launched power and a density of 2.5×10^{19} m^{-3} with inductive compensation of the EC-driven current to maintain net current free conditions, $I_{\mathrm{ind}} + I_{\mathrm{boot}} + I_{\mathrm{ECCD}} = 0$ (I_{ind} is the inductive component, I_{boot} and I_{ECCD} are the bootstrap and the EC-driven components, respectively). The microwaves were injected from the low-field side in X2 mode polarization, and the polarization was adjusted according to the given launch angle from linear to elliptical polarization to provide optimum coupling of the microwaves. During the scan, the toroidal magnetic field was adjusted to keep the Doppler-shifted deposition profile close to the plasma axis ($\Delta B/B \cong 10\%$ for $|\varphi_{\mathrm{inj}}| = 30°$). Under these conditions, ray-tracing calculations predict a peaked deposition profile with flux-surface-averaged

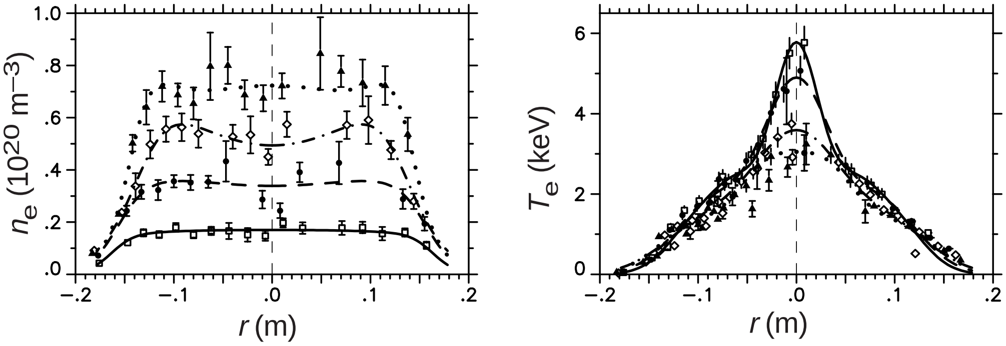

Fig. 1. Radial profiles of the electron density (left) and temperature (right) with 1.2 MW of ECRH.

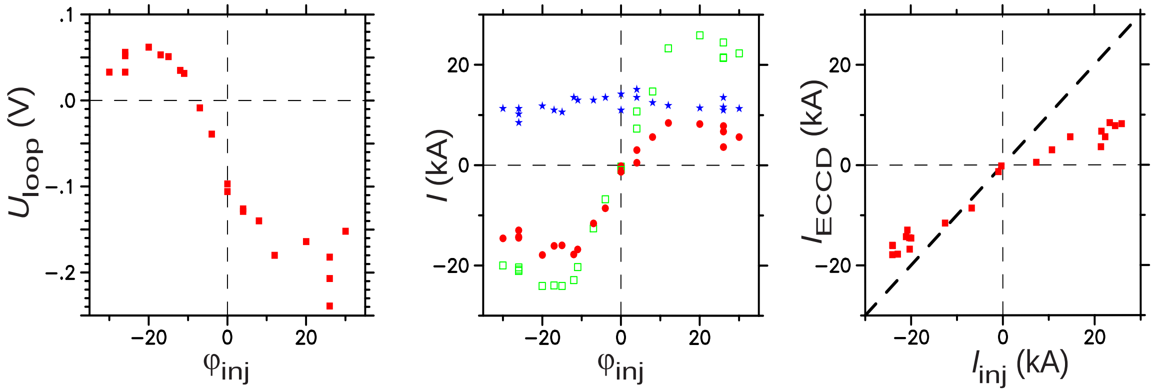

Fig. 2. Left: Loop voltage vs toroidal angle of injection in net current- free discharges, $U_{\mathrm{loop}} = -(I_{\mathrm{boot}} + I_{\mathrm{ECCD}})/R$. Perpendicular injection corresponds to $\varphi_{\mathrm{inj}} = 0°$. Center: Theory (open squares) and data from current balance of the EC-driven current (dots) together with the bootstrap current (stars) as a function of the launch angle. Right: EC-driven current from current balance vs linear prediction.

power densities of up to 50 MW/m^3. The required inductive loop voltage for current compensation is shown in Fig. 2 (left) as a function of the launch angle φ_{inj} ($\varphi_{\mathrm{inj}} = 0°$ corresponds to perpendicular injection, $I_{\mathrm{ECCD}} = 0$). For a quantitative comparison of the measured data with theory we assume a linear superposition of the three current contributions, which is justified because the suprathermal electrons generated by ECRH have only a negligible effect on the electric conductivity as confirmed by Fokker-Planck calculations [5]. The bootstrap current is calculated with the DKES code, taking into account the ambipolar radial electric field, and the inductive current is calculated assuming neoclassical resistivity (effective charge Z_{eff} = 3–6). The calculations are performed for each individual discharge using the measured profiles of n_e and T_e. Then the EC-driven current from the current balance $I_{\mathrm{ECCD}} = -I_{\mathrm{ind}} - I_{\mathrm{boot}}$ is plotted as in Fig. 2 and compared with the linear theoretical ECCD current, I_{inj}. The maximum linear ECCD efficiency from ray tracing (based on the adjoint approach with trapped particles [6] included), $\eta_{\mathrm{ECCD}} \cong$ 20 A/kW, corresponds to a normalized efficiency $\gamma_{\mathrm{ECRH}} = n_e I_{\mathrm{ECCD}} R / P_{\mathrm{ECRH}} \cong 0.01 \times 10^{20}$ A/Wm^2.

As seen in Fig. 2 (right), where the “experimental” I_{ECCD} is plotted vs theory, good agreement with linear theory is observed even at these extremely high power densities except for launch angles in the co-direction. This may hint at a degradation of the CD efficiency at high power density. The calculations of both the inductive current and the bootstrap current are very conservative and are expected to be more reliable than the linear ECCD calculations, where the assumptions of the linear approach are likely to be violated. Nonlinear effects in the wave-particle interaction in an inhomogeneous magnetic field are important, especially at moderate launch angles. Thus the quasilinear theory, which holds in a homogenous magnetic field, must be reformulated. In addition, the wave absorption increases the perpendicular energy and pushes electrons into the loss cone. In the bounce-averaged Fokker-Planck calculation the strong heating as formulated by the traditional quasilinear diffusion term is balanced by the energy loss of mainly suprathermal ripple-trapped electrons. The radial ∇B drift of suprathermal ripple-trapped electrons broadens the power deposition profile [3] but has no influence on the ECCD profile. In the electron distribution function, however, positive gradients with respect to $v_{\|}$ close to the loss-cone boundary are found; these represent free energy and may drive the distribution function unstable. The fast growth rate of such kinetic instabilities affects the distribution function and can reduce the CD efficiency, which would again require a reformulation of Fokker-Planck modeling.

In discharges with strong co-CD, MHD activity is observed; it is absent in the counter-CD cases. This is explained by the strong change in the radial profile of the rotational transform while scanning from co- to counter-CD, because the different current contributions flow at different radial positions. The bootstrap current is localized in the pressure gradient region, whereas the inductive current follows the plasma conductivity profile and the EC-driven current is localized around the resonance. Figure 3 shows radial profiles of T_e with the rotational transform for co- and counter-CD.

For co-CD the temperature profiles remain peaked and the ɨ profile crosses the ɨ = 1/3 and ɨ = 1/2 surfaces with strong shear. The observed MHD modes are the corresponding m = 3 and m = 2 modes, which may influence the current distribution. The modes are located around the rational ɨ values as measured by ECE, soft X-ray and Mirnov diagnostics. In the opposite case of counter-CD, the ɨ = 0 surface appears in the plasma center and the temperature profile is flat within this surface, indicating bad or no confinement within this surface. In consequence, the EC-

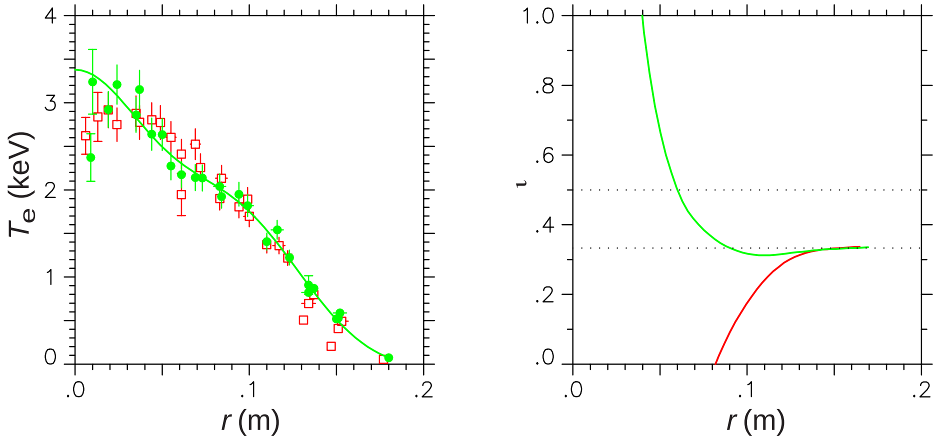

Fig. 3. Radial profiles of the electron temperature T_e (left) and rotational transform ι (right) for co- (dashed line) and counter-CD (solid line) at zero net-current, φ_{inj} = + and – 12°, respectively.

driven current within the ι = 0 surface may be distributed over a wider volume than calculated by ray tracing, leading to a reduced power density, a lower deviation from a Maxwellian distribution function, and thus a better agreement with linear CD theory.

Conclusions

Experiments with ECRH and ECCD were performed on W7-AS with enhanced heating power, which is well beyond the previous frame of investigations. New physics appears in the experiments and drives theory into the interpretation of strong kinetic effects. The central confinement of ECR-heated discharges is strongly influenced by ECRH- specific features. Positive radial electric fields driven by fast electron losses in the plasma center (electron root) provide significantly enhanced electron confinement, resulting in peak temperatures of 5.7 keV.

Net current-free discharges with up to 20 kA of highly localized EC-driven currents in the co- and counter-directions to the bootstrap current were investigated and compared with linear predictions. The experiments indicate a deviation from linear ECCD theory under some conditions, which calls for advanced kinetic modeling.

The radial profile of the rotatational transform was tailored by strong ECCD over a wide range. This includes tokamak-like profiles, which exhibit rational resonances of ι with related MHD activity, and inverse profiles, where ι = 0 and bad confinement or no confinement appears in the inner plasma region.

V. Erckmann and H. Maassberg for the W7-AS Team and the ECRH Group at Institut für Plasmaforschung, Stuttgart

References

[1] V. Erckmann and U. Gasparino, “Electron Cyclotron Resonance Heating and Current Drive in toroidal Fusion Plasmas,” Plasma Phys. Controlled Fusion **36**, 1869 (1994).

[2] M. Romé, V. Erckmann, U. Gasparino, H. J. Hartfuss, G. Kühner, H. Maassberg, and N. Marushchenko, “Kinetic modeling of the ECRH power deposition in W7-AS,” Plasma Phys. Controlled Fusion **39**, 117 (1997).

[3] S. Murakami, U. Gasparino, H. Idei, S. Kubo, H. Maassberg, N. Marushchenko, N. Nakajima, M. Romé, and M. Okamoto, “5D Simulation study of suprathermal electron transport in non-axisymmetric plasmas,” Paper IAEA-CN-69/TH2/1 (R) THP1/1, presented at 17th IAEA Fusion Energy Conference (Yokohama, 1998), to be published in the proceedings (1998).

[4] H. Maassberg, C. D. Beidler, K. S. Dyabilin, U. Gasparino, S. Murakami, and W7-AS Team, “The neoclassical electron root feature in the W7-AS stellarator,” submitted to Plasma Phys. Controlled Fusion.

[5] N. Marushchenko., U. Gasparino, H. Maassberg, and M. Romé, “Bounce averaged Fokker-Planck code for the description of ECRH in a periodic magnetic field,” Comput. Phys. Commun **103**, 145 (1997).

[6] M. Romé, V. Erckmann, U. Gasparino, and N. Karulin, “Electron cyclotron resonance heating and current drive in the W7-X stellarator,” Plasma Phys. Controlled Fusion **40** 511 (1998).

Electron Bernstein wave heating and emission via the OXB process on W7-AS

The maximum density at which electron cyclotron (EC) waves can be used for heating and diagnostics is usually limited by the plasma cut-off density.

In addition to the well-known electromagnetic EC waves, there exists an electrostatic EC wave, the electron Bernstein (EB) wave. For this wave no upper density limit exists, but propagation is only possible above a threshold density. Therefore EB waves cannot be excited from the vacuum, but have to be generated via mode conversion from the electromagnetic waves.

One possible method of achieving this is the so-called OXB process, which was proposed by J. Preinhaelter and V. Kopeck for electron cyclotron resonance heating (ECRH) [1]. This process is a general physics phenomenon of EC waves propagating in hot magnetized plasmas, such as ionospheric or fusion plasmas. Here O, X, and B represent the ordinary, extraordinary, and the electron Bernstein modes. As shown in Fig. 1, the transverse refractive indices $N_\perp$ of the O-wave and X-wave along a wave trajectory in a density gradient are connected at the optimal launch angle φ without passing through a region of evanescence ($N_\perp^2 < 0$) at the O-mode cut-off. Here in a first step an O-wave is converted into a slow X-wave. In a second mode conversion step an EB wave is generated from the slow X-wave at the upper hybrid resonance (UHR), where the X-mode branch of the solution of the hot plasma dispersion relation is connected to the EB branch.

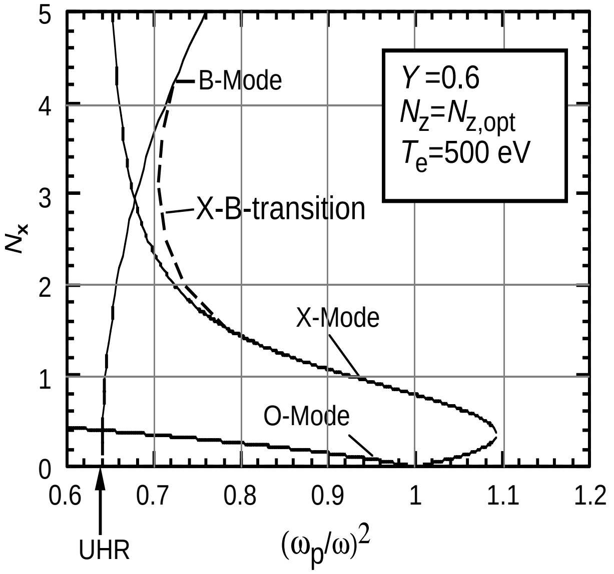

Fig. 1. Refractive index $N_\perp$ vs ω_p^2/ω^2 for the OXB conversion process. The transition represents the connection of the X-mode and B-mode resulting from the hot dielectric tensor.

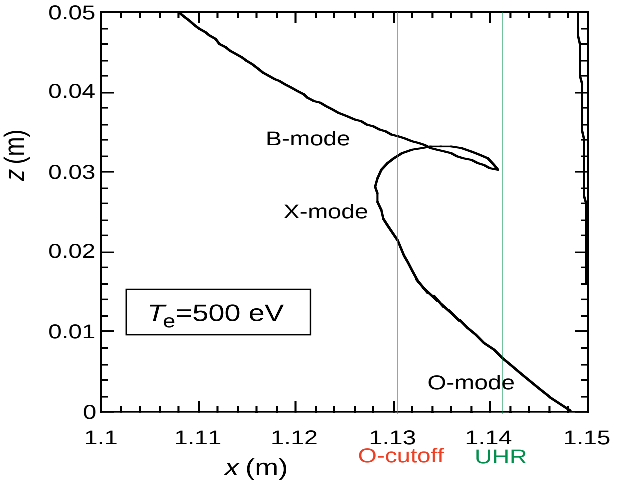

Fig. 2. Results of ray tracing calculations. Ray trajectory in the density gradient region near the plasma edge for a magnetic field of 2.2 T. The plasma edge was assumed at x = 1.15. The ray was launched from the vacuum with a launch angle φ = 47°. The density is increasing to the left side.

For EB waves no density limit exists; they propagate towards the dense plasma center, where they are absorbed by cyclotron damping. Both mode conversions are reversible; thus, the BXO process can also take place.

The mode conversion process requires an optimal parallel component $N_{||}$ of the refractive index vector or, equivalently, an oblique launch toroidal angle φ for heating or detection near an optimal angle φ for EB wave emission (EBE). Further, a plasma density above the O-wave cut-off and a frequency above the first cyclotron harmonic in the plasma are necessary.

In Fig. 2, ray trajectories in the equatorial plane were calculated by a ray-tracing code for the mode conversion region near the plasma edge. Since at the cyclotron resonance the plasma is optically thick for the EB waves, it is a blackbody emitter for EB waves just as it is for electromagnetic EC waves below the cut-off density. In contrast to electromagnetic waves, EB waves generally cannot leave the plasma since they have a density threshold for propagation at the UHR, which totally encloses the inner part of the plasma. Indeed, at the UHR they can be converted into slow X-waves, but these are also unable to leave the plasma and are backconverted to EB waves at their next contact with the UHR surface.

The EB wave radiation is trapped inside the plasma as though in a hohlraum, except for those EB waves which

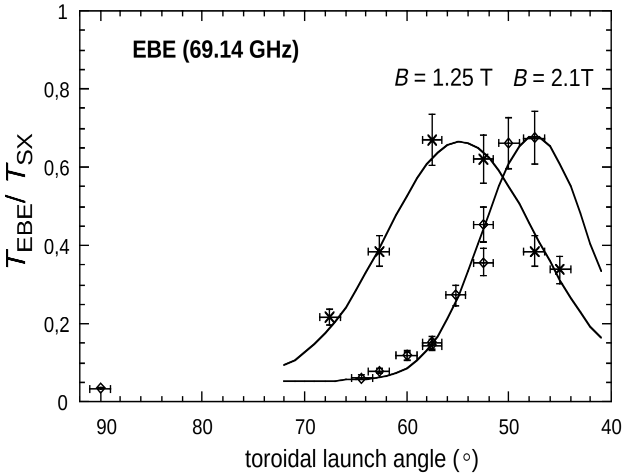

Fig. 3. Angular dependence of EBE for different central magnetic fields, for central density of 1×10^{20} m^{-3} and temperature of 600 eV. The signal is normalized to the central soft-X temperature.

are "born" with an optimal $N_{||}$ (parallel to the magnetic field) for the BXO process (local emission). EB waves that achieve such an $N_{||}$ component on their way through the plasma by scattering or magnetic configuration effects such as the field line curvature are able to leave the plasma (nonlocal "hohlraum" emission).

The optimal $N_{||}$ and the optimal launch and viewing angle φ respectively are defined by the following relation [1]: $N^2_{||,\mathrm{opt}} = \cos^2(\varphi) = Y/(Y+1)$ with $Y = \omega_{ce}/\omega$ (ω is the wave frequency, and ω_{ce} is the electron cyclotron frequency). In a three-dimensional plasma one has also to take into account the perpendicular (poloidal) refractive index N_y or the poloidal angle θ, but in our experiments no variation of N_y was performed. The shape of the angular window or the transmission function $T(N_y, N_{||})$ depends on the density scale length $L = n_e/(\partial n_e/\partial x)$ and is given by Mjølhus [2] with

$$T(N_y, N_{||}) = \exp\left\{-\pi k_0 L \sqrt{\frac{Y}{2}}[2(1+Y)(N_{||,\mathrm{opt}} - N_{||})^2 + N_y^2]\right\},$$

where k_0 is the wave number.

This angular dependence ($N_{||}$ dependence) of the mode conversion was used in the experiments, among other criteria, to identify EB wave heating and emission. Another criterion is the density threshold of the OXB and BXO processes, which can only takes place if the density is above the O-mode cut-off density of the emitted frequency. Finally, for the heating experiments a special footprint for the XB conversion: the parametric decay of a part of the launched waves due to the strong nonlinearity and the high power density at the UHR where the XB mode conversion takes place.

Experiments

The heating experiments were performed on the W7-AS stellarator with two 70-GHz gyrotrons, each with 110 kW of power. The central magnetic field was set between 1.25 and 2.5 T and the edge rotational transform near 0.35 according to the experimental requirements. The central density of the neutral beam injection (NBI)-sustained target plasma was up to 1.6×10^{20} m^{-3}, which is more than twice the 70-GHz O-mode cut-off density. Co- and counter NBI with 360 kW power each were used to compensate for the momentum transfer to the plasma.

For the EB wave emission measurement, the W7-AS ECE radiometers were connected to an unused movable ECRH launch antenna.

Variation of the launch angle

The launch angle of the incident O-mode polarized wave was varied at fixed heating power (220 kW) in a nonresonant magnetic field. The increase of the total stored plasma energy (from the diamagnetic signal) depends strongly on the launch angle, which is typical for the OX conversion process, and fits well to the calculation. The plasma energy content increased by about 1.5 kJ compared to a similar discharge with NBI only. More than 70% of the heating power was found in the plasma if the power scaling of the energy confinement ($P^{-0.6}$) was taken into account. Thus OXB-heating turned out to be efficient.

Scans of the viewing angle were performed for the first and second harmonic EB emission (EBE) as shown in Fig. 3, and the predicted angular windows at 47° for 2.1 T (69.14 GHz) and 55° for second harmonic EBE at 1.25 T could be experimentally reproduced. The radiation temperature was up to 70% of the temperature measured by soft X-ray emission and Thomson scattering. This might be due to reduced XO conversion caused by density fluctuations at the cut-off surface as described in Ref. [3].

Density variation and parametric instability

These experiments were designed to demonstrate, that a density threshold (O-mode cut-off) for the OX conversion exists and that the parametric decay process which is a characteristic of the XB conversion takes place. For this the plasma was built up by one 70-GHz gyrotron in X-polarization in a resonant central magnetic field of 1.25 T. Then the density was slowly ramped up to density above the O-mode cut-off. In parallel, as shown in Fig. 4, a second 70-GHz beam, O-mode polarized with the optimal launch angle and modulated with 20% amplitude, was launched into the plasma. During the plasma buildup thermal EC emission (ECE) was detected. As soon as the cut-off density was reached, ECE vanished and OXB heating started, which caused an increase of the plasma energy and central soft x-ray emission. Simultaneously the parametric instability (PI) at the XB conversion process generated a

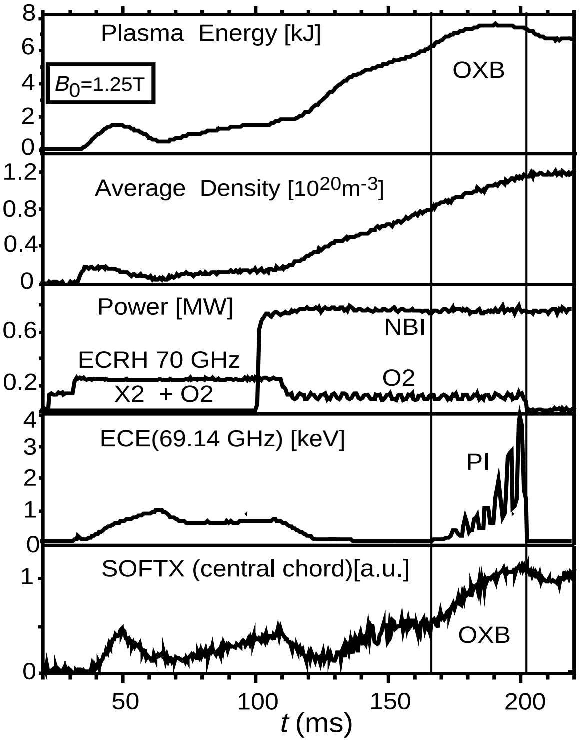

Fig. 4. Temporal development of some plasma parameters during an OXB-heated discharge. From the top: plasma energy estimated from the diamagnetic signal, average density from the interferometric measurement, heating power, intensity of ECE and PI, central soft X-ray signal. The markers show the OXB heating interval.

decay spectrum, whose high-frequency part could be measured with the ECE detector. The modulation amplitude strongly exceeded that of the pump wave, clearly demonstrating the nonlinear character (power threshold) of the PI. Figure 5 shows the high-frequency decay spectrum. Two red-shifted lines and one blue-shifted line can be recognized. Their spectral distances to the 70-GHz pump wave, which was suppressed by a notch filter, are multiples of the lower hybrid resonance (LHR) frequency (~900 MHz). The spectrum of the LHR oscillation itself could be detected by a loop antenna. The LHR oscillation shows a high degree of correlation with the high-frequency decay waves.

For the emission measurement, the receiving mirror was turned to the optimum viewing angle of 47° with respect to the magnetic field and the plasma density was ramped up to above the cut-off density, as shown in Fig. 6. The plasma was sustained by two neutral beam injectors, each with 360-kW power. The central magnetic field was set to 2.1 T to compensate for the Doppler shift of the EBE spectrum. For comparison the plasma temperature measured with the soft X-ray filter method for the central line of sight is plotted at the top of Fig. 6. Below, the low-field-

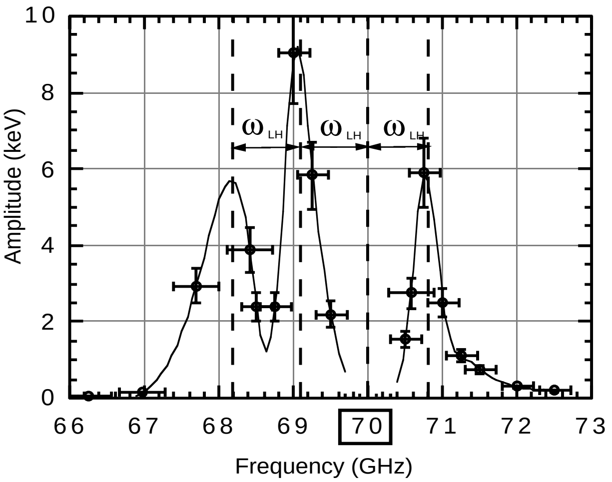

Fig. 5. High-frequency spectrum of the parametric decay waves generated in the XB process. The incident wave frequency is 70 GHz, and the lower hybrid frequency is about 900 MHz.

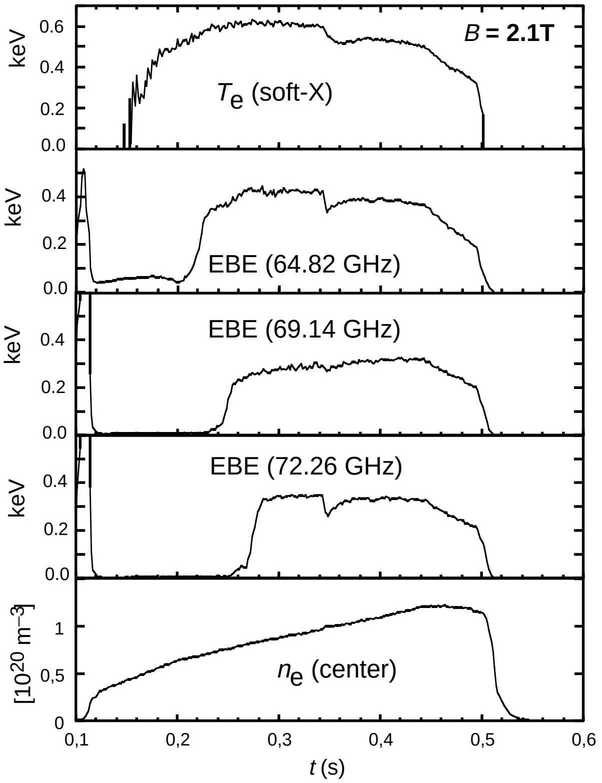

Fig. 6. Signals of an NBI-sustained discharge with a density ramp. From the top: soft-X-ray temperature; radiation temperature of the low-field-side edge EBE, central EBE, and high-field-side edge EBE; and central density. The temperature dip at 0.34 s is due to a perturbation induced by carbon laser blowoff.

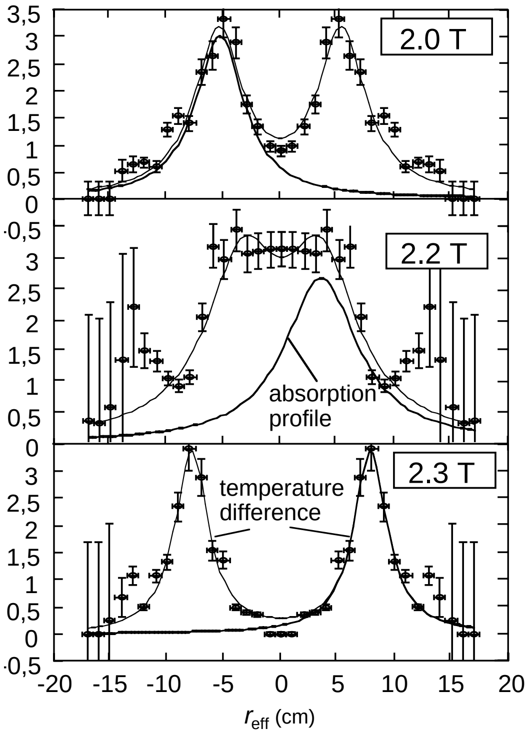

Fig. 7. Changes of temperature 3 ms after OXB heating switch-off and related ECRH absorption profiles for different central magnetic fields.

side EBE radiation, the central EBE, and the high-field-side EBE are shown. When the central density as measured with a microwave interferometer and by Thomson scattering reaches the cut-off density of the emitting frequency, the BXO window opens and EBE appears. Note, that the soft X-ray temperature measurement is not a local one.

Resonant cyclotron absorption and local EB wave emission

For the heating the central magnetic field was varied between 2.0 T and 2.5 T to show resonant absorption of the EB waves. In the equatorial plane the magnetic field as a function of the effective radius r_{eff} is approximately given by

$$B(r_{\text{eff}}) = (B_0 A)/(A + r_{\text{eff}}/a)$$

with $A = 10.5$. The power deposition was estimated from the change of the temperature profile at the power switch-off. Since the density was far above the ECE cut-off, the temperature profiles were calculated from the soft X-ray emission and the Thomson scattering diagnostic. The central temperature was 500 eV. The X-ray emission was monitored by an array of 36 silicon detectors with a 25–μm beryllium filter. To obtain the radial X-ray emission profile, the signals were inverted to the magnetic flux coordinates. The time resolution was 0.1 ms and the radial resolution was about 1 cm.

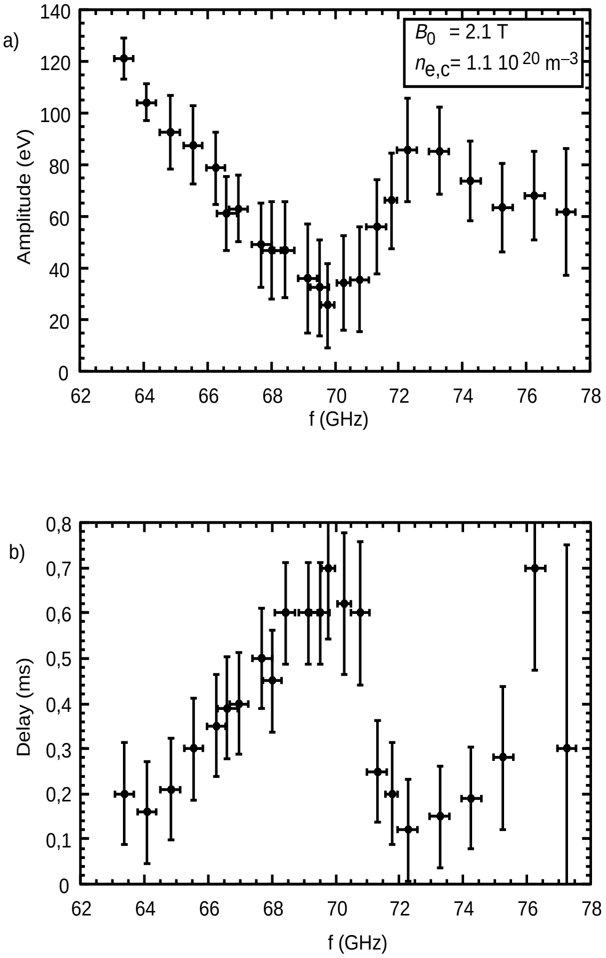

Fig. 8. (a) Amplitude decay and (b) delay time of the $1/e$ amplitude as a function of EBE frequency. The inward propagation of the temperature perturbation is induced by carbon laser blowoff at the plasma edge, thus demonstrating the localization of the radiation origin.

In Fig. 7 the absorption profiles for different magnetic fields are shown. The absorption is strongly Doppler shifted owing to the oblique launch and moves from the high-field side at 2.0 T through the center (2.2 T) to the low-field side at 2.3 T with increasing magnetic field, which clearly demonstrates the propagation and the local cyclotron absorption of the EB waves. No significant difference in heating efficiency between resonant and nonresonant heating could be detected. The heating efficiency is mainly determined by the OX conversion conditions at the plasma edge, as reported in Ref. [2].

To establish a relation between the frequency of the thermal EBE and the radial position of the emission zone. Temperature perturbations at the plasma edge were created by carbon laser blow off. The amount of ablated carbon was selected to cause a sufficiently large temperature decrease in all EBE channels, but with a minimum disturbance of the plasma discharge, especially with no signifi-

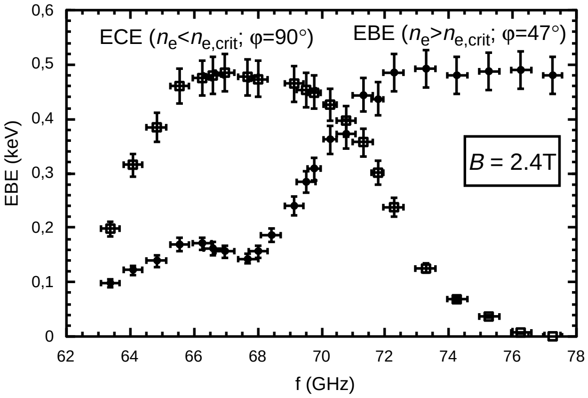

Fig. 9. Doppler-shifted EBE spectrum (circles) and ECE spectrum for similar discharges but at different densities (squares). In the EBE discharge, the central temperature was 700 eV.

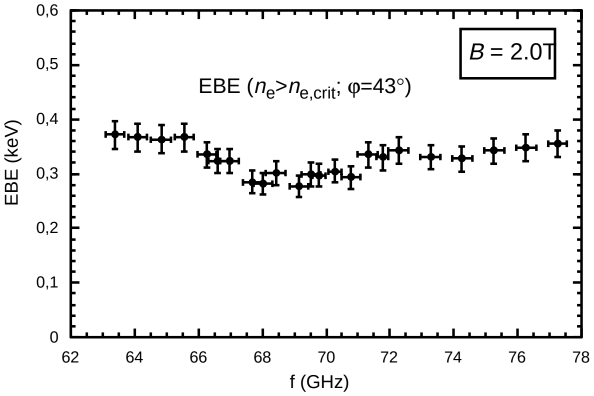

Fig. 10. High-frequency part of the EBE spectrum. The central EC resonance frequency is shifted by about 11.2 GHz with respect to Fig. 4. Owing to the confinement degradation with decreasing magnetic field, the central temperature decreases to about 500 eV.

cant density increase. An example is shown in Fig. 6, where the cold pulse was set at 0.34 s. One could identify a steep temperature dip in the edge EBE channels (64.84 GHz, 72.26 GHz), a small dip in the central channel (69.14 GHz), and almost no change in the average plasma density.

In Fig. 8 the amplitude and the delay time in which the signal reaches 1/*e* of the amplitude of the cold pulse are plotted as a function of the emission frequency. Assuming that the cold pulse propagates from the outer radii towards the center, both the amplitude and the delay time indicate that for the thermal part of the spectrum there is a clear relation between the emitted frequency and the radial position of the emission. For the spectrum above 73 GHz, no amplitude variation and no clear phase attachment could be found, which indicates the nonlocal character of the high-frequency part of the EBE.

The EBE spectrum

ECE and EBE spectra were compared. The central magnetic field was set at 2.4 T, for which both spectra are in the spectral range of our detection system (61–78 GHz). As shown in Fig. 9, both the thermal ECE spectrum (first harmonic O-mode, $n_e < n_{e,cut\text{-}off}$, squares) received by the ECRH antenna with 90° viewing angle and the EBE spectrum at 47° (first harmonic, $n_e > n_{e,cut\text{-}off}$, circles) of an NBI-sustained plasma are shown. The ECE spectrum reflects the plasma temperature profile. The EBE spectrum is about 6 GHz Doppler shifted and shows the low-field (frequency)-side temperature gradient. The small pedestal at its low-frequency part may originate from stray radiation emitted at the low-density plasma edge. In order to record also the high-frequency part of the spectrum, the magnetic field was reduced by 0.4 T corresponding to a central EC resonance frequency of 11.2 GHz.

As shown in Fig. 10, instead of a high-field-side decay as is typical for ECE, the EBE spectrum has a slowly decreasing broadband high-frequency part. By a further shift of the EC resonance frequency we found that the high frequency part is emitted up to about 1.7 times the EC frequencies in the plasma. We suppose that this is the nonlocal “hohlraum” radiation, as discussed above.

Summary and Conclusions

EC heating of an overdense plasma with 70-GHz EB waves was clearly demonstrated on W7-AS [3]. The EB waves were generated via mode conversion in the OXB process. Both the angular dependence of the OX conversion and the PI which is typical for XB conversion could be experimentally verified. The position of the narrow absorption profile, estimated from the soft X-ray emission, could be changed by a shift of the cyclotron resonance layer. Thus generation, propagation, and local resonant cyclotron absorption of EB waves were shown.

The inverse process, EB wave emission through the OXB mode conversion window from an overdense plasma, was detected with an oblique observation angle [4]. The emitted spectrum consists of two parts.

The thermal part reflects the local thermal emission of EB waves, and in principle a radial temperature can be reconstructed from this radiation. The high-frequency part represents nonlocal “hohlraum” radiation since most of the EB waves are trapped inside the plasma and only those rays which somehow obtain the optimal $N_{||}$ and N_y for the small angular window of the BXO process can leave the plasma.

Both the local and nonlocal character of the EBE spectrum were demonstrated by cold wave propagation with laser blowoff.

Besides the renewed verification of the hot plasma wave theory and the insight into EB wave physics in a fusion plasma, the OXB process opens also a new operational window for EC heating and EC diagnostics beyond the cut-off, for fusion as well as for ionospheric research.

H.P. Laqua, W7-AS Team
Max-Planck-Institut für Plasmaphysik
EURATOM Association
D-85748 Garching, Germany
ECRH Group
Institut für Plasmaforschung, Univ. Stuttgart
D-70569 Stuttgart, Germany

References

[1] J. Preinhaelter and V. Kopeck, J. Plasma Phys. **10**, 1 (1973).

[2] E. Mjølhus, J. Plasma Phys. **31,** 7 (1984).

[3] H. P. Laqua et al., Phys. Ref. Lett. **78**, 18 (1997).

[4] H. P. Laqua et al., Phys. Ref. Lett. **81**, 10 (1998).

Computational study of toroidal Alfvén eigenmodes in W7-AS

The diagnostic methods used in the Wendelstein 7-AS (W7-AS) magnetic confinement experiment to measure and reconstruct magnetohydrodynamic (MHD) activity, have developed to a stage where precise information on the frequencies as well as the spatial structures of such activity can be given. A solid basis for a computational study of these phenomena exists, since (1) very good agreement has been obtained from the comparison of soft X-ray tomographic equilibrium measurements of W7-AS discharges [1, 2] with computational reconstruction [3, 4] using the NEMEC 3-D MHD equilibrium code [5], and (2) the full ideal MHD stability problem in general 3-D toroidal geometry can be studied with the CAS3D3 version of the finite-element Fourier code package CAS3D (Code for the Analysis of the MHD Stability of 3-D Equilibria) [6, 7].

The soft X-ray diagnostic system MiniSoX has also been successfully used to measure and describe the various types of MHD activities observed in neutral-beam-heated plasmas of W7-AS [1], such as global Alfvén eigenmodes (GAEs) and toroidal Alfvén eigenmodes (TAEs). Here, a comparison of soft X-ray measurement and CAS3D computations will be described for a neutral-beam-heated discharge with moderate shear (shot 39042) that is typical of the presence of TAEs.

Structure of stable ideal MHD spectra

An analytical derivation in the straight-cylinder limit shows the existence of the sound and the Alfvén continua, which consist of completely decoupled branches given by their poloidal and toroidal Fourier indices. The structure of the ideal MHD spectrum changes considerably when a simple cylinder is distorted into geometrically more complicated configurations (tokamaks and stellarators), in which the decoupling of the perturbation Fourier harmonics is applicable only to a certain extent. In these cases a crossing-over of Alfvén branches which belong to different Fourier numbers and which are geometrically coupled does not occur; instead a spectral gap forms. Furthermore, discrete eigenvalues can be found within the gaps: the corresponding smooth eigenfunctions are called gap modes. TAEs, for example, reside in gaps generated by the interaction of continuum branches, which are coupled by the main toroidal equilibrium terms.

Because of the 3-D formulation employed, all geometry-induced and plasma beta-induced mechanisms for gap formation are automatically present in a CAS3D calculation. Calculations for tokamak equilibria recover all the typical properties of the stable MHD spectrum, such as the exist-

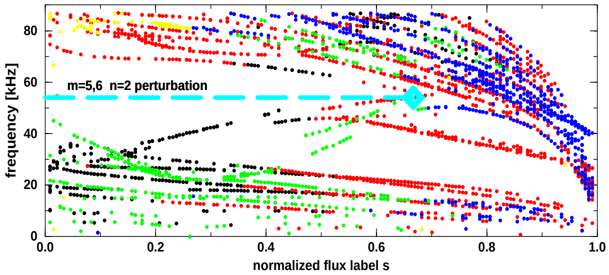

Fig. 1. The lower part of the stable MHD spectrum as obtained from CAS3D3 for perturbations of the $n = 2$ mode family in W7-AS discharge #39042. Computation parameters: 162 radial grid points, 40 Fourier harmonics for each of the 3 scalar perturbation functions, $\gamma = 2$. Color code: (5,–2), black,;(6,–2), red; (8,–3), green; (9,–3), blue.

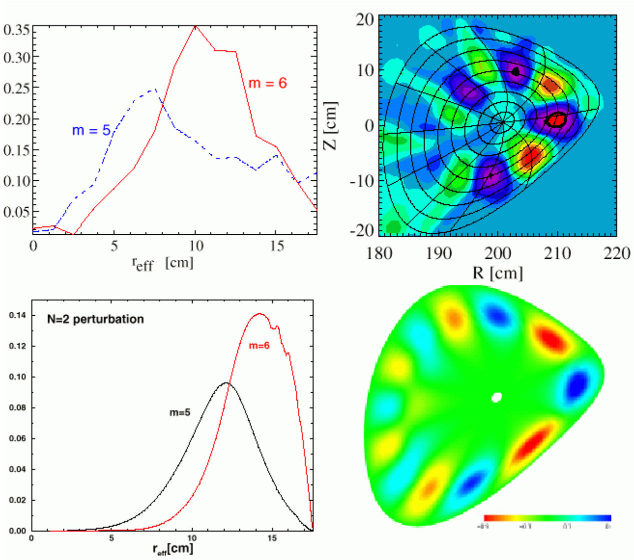

Fig. 2. Comparison of soft X-ray measurement (top row, 47 kHz) and CAS3D3 (54 kHz) results: The left column shows the (5,–2) and (6,–2) Fourier harmonics of the normal displacement versus effective radius. The right column gives the spatial structure of the perturbation as found with the soft X-ray diagnostic and the perturbed pressure as given by CAS3D3.

minor radius	***a* (m)**	**0.1753**
major radius	***R* (m)**	**1.8682**
magnetic field	***B*(T)**	**2.57**
plasma-β	**⟨β⟩**	**0.00255**
electron density	**$n_e(0)$ (10^{20} m^{-3})**	**1.242**
Alfven velocity	**$v_A(0)$ (10^7 m/s)**	**0.41**

Table 1. MHD-relevant parameters for the W7-AS discharges that were selected for computational reconstruction with CAS3D.

ence of spectral gaps and gap modes. For 3-D equilibria non-tokamak-type effects can also influence the structure of the stable spectrum; for example, the formation of helicity-induced gaps has been observed in W7-X-type cases [7]. Gap formation in the sound spectrum and between branches of the sound and Alfvén spectra in the case of overlap were also demonstrated with the CAS3D code.

Alfvén eigenmodes in W7-AS

In W7-AS shot 39042, the rotational transform profile decreases from 0.39 on the magnetic axis to 0.34 on the plasma boundary (see Table 1 for other parameters). The experimental soft X-ray analysis detects an $m = 5,6$ TAE mode at a frequency of 47 kHz. The lower part of the stable spectrum of discharge 39042 has been studied with the CAS3D code for perturbations belonging to the $n = 2$ mode family. Figure 1 shows the resulting CAS3D spectrum with the various sound and Alfvén continuum branches and the formation of gaps. The spectral gaps are toroidicity induced, since they originate from the coupling of the (5,–2) and (6,–2) and, similarly, of the (8,–3) and (9,–3) Alfvén branches, which is caused by the (1,0) component of the equilibrium quantities (representing the toroidal effect).

Various global modes can be found with $n = 2$ dominant toroidal Fourier harmonics. The three prominent types of global modes that appear all have the same dominant Fourier contents; they differ in their radial behavior. *Ballooning-type* or even modes, those with their dominant amplitudes on the outside of the torus, are present with no or several radial nodes. With higher frequency *anti-ballooning-type* perturbations could also be found; these have their maximum amplitude on the inside of the torus. For these perturbations the dominant Fourier harmonics are of opposite sign; they are so-called odd modes. The corresponding, dominantly $n = 3$ modes are also present.

Figure 2 compares soft X-ray measurements and CAS3D3 results for this TAE case. The main features of the experimentally observed MHD activity are well represented by the computation. The soft X-ray frequency (47 kHz) and the CAS3D frequency (54 kHz) compare well, especially if this experimental frequency is corrected for Doppler shift effects. There are slight discrepancies in the spatial structure. The outward radial shift, which is present in the CAS3D results, can possibly be attributed to uncertainties in the mass density profile and the numerical modeling of the discharge.

Carolin Nührenberg
Max-Planck-Institut für Plasmaphysik
EURATOM Association
D-17489 Greifswald, Germany

Joachim Geiger, Caio Görner, and Arthur Weller[2]
Max-Planck-Institut für Plasmaphysik
EURATOM Association
D-85748 Garching, Germany

References

[1] C. Görner, M. Anton, J. Geiger, W. von der Linden, A. Weller, S. Zoletnik, and the W7AS-Team, in *Proc. 24th European Conf. Controlled Fusion Plasma Phys.* (Berchtesgaden 1997), Eur. Conf. Abstr. **21A**, IV, 1625 (1997).

[2] *Stellarator News*, Issue 55, January 1998.

[3] H. Callaghan, J. Geiger, et al., in *Proc. 24th European Conf. Controlled Fusion Plasma Phys.* (Berchtesgaden 1997), Eur. Conf. Abstr. **21A**, IV, 1617 (1997).

[4] *Stellarator News*, Issue 53, September 1997.

[5] S. P. Hirshman, W. I. van Rij, and P. Merkel, Comput. Phys. Commun. **43**, 143 (1986).

[6] C. Nührenberg, Phys. Plasmas **3**, 2401 (1996).

[7] C. Nührenberg, Phys. Plasmas, in press (January 1999).

Energetic particle-driven Alfvén instabilities in W7-AS

Neutral-beam-driven Alfvén eigenmodes are the most striking MHD instabilities in W7-AS, and therefore continuous efforts are made to study their characteristics and their relevance for fast particle confinement. The advanced stellarator configuration of W7-AS, characterized by very low shear (~10%), large aspect ratio (~10), and a particular 3-D field geometry, leads to an Alfvén spectrum that differs from that of conventional tokamaks and high-shear stellarators. In particular, low shear causes toroidal Alfvén eigenmode (TAE) gaps to disappear and results in the appearance of weakly damped global Alfvén eigenmodes (GAEs) below the Alfvén continua with frequencies $\omega_{GAE} = (k_{\|} \cdot v_A)_{min}$, which are excited through resonances with fast passing particles from NBI.

The basic features of the low-frequency (< 50-kHz) GAE modes have been consistently described by an MHD code with a gyrofluid model for the fast beam ions (neglecting 3-D effects of the magnetic field) [1], and initial 3-D MHD calculations of the stable part of the ideal MHD spectrum have been performed with the CAS3D code for selected W7-AS cases [2]. For interpretation of the results and comparison with code calculations, analysis of the mode structure is important. We investigate the mode structure using a soft X-ray tomography system (10 cameras, 320 channels) [3]. An example for tomographic reconstructions of GAE mode structures is shown in Fig. 1, for a shot in which several GAE modes of different poloidal and radial structure occurred simultaneously.

In W7-AS shear is generated to some extent by Pfirsch-Schlüter, bootstrap, and NBI-driven currents, which are usually compensated for by OH-driven currents. Small amounts of shear lead to stabilization of GAEs, as inferred from cases with different plasma beta. Calculations show that increased continuum damping may cause the stabilization. We have used OH current drive to change the shear,

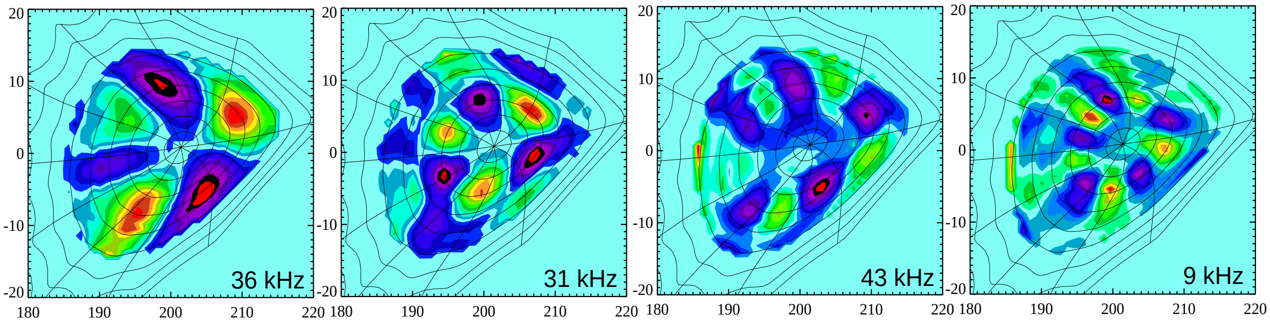

Fig. 1. X-ray tomograms of $m = 3$ and $m = 5$ GAE modes of different frequencies. The modes appear simultaneously (W7-AS shot 39029) and are separated by Fourier filtering.

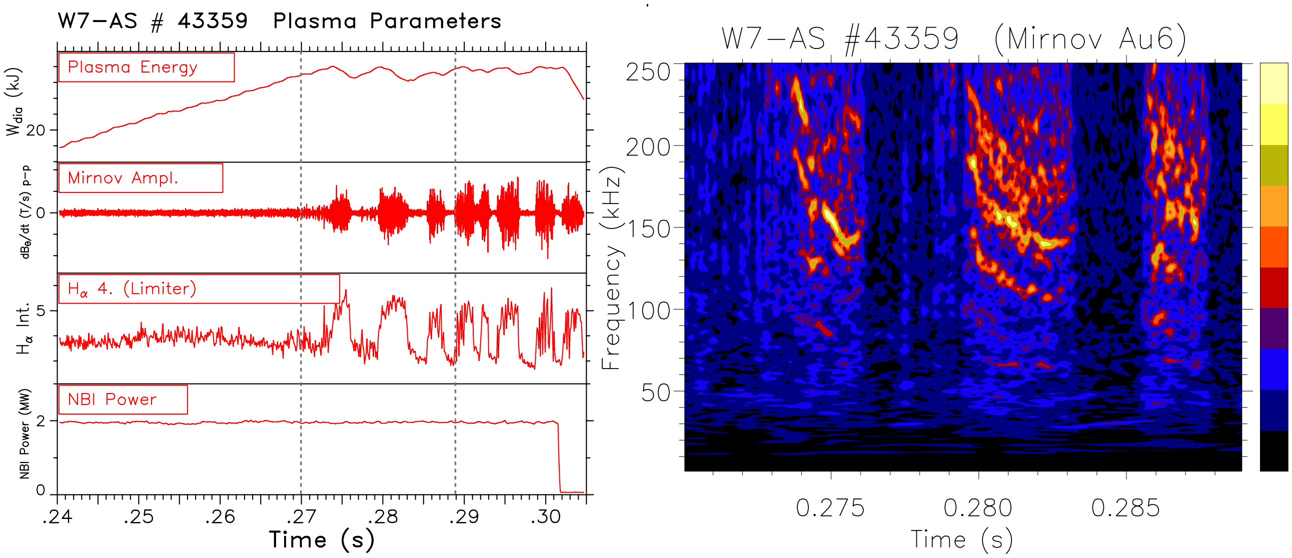

Fig. 2. Effect of higher frequency intermittent GAE activity on confinement under conditions where $v_A < v_{beam,max}$ (intermediate NBI power, density, and beta). Left: diamagnetic energy, Mirnov signal, H_α signal, NBI power. Right: wavelet spectrogram of the Mirnov signal. Frequency chirping is observed during the MHD bursts, which are correlated with plasma losses.

including cases with positive and negative shear. Although global plasma parameters, and therefore drive and damping effects, depend on the iota profile, the changes of the mode behavior seem to be in qualitative agreement with expectations on the basis of the modifications of the Alfvén continua. In particular, at higher shear TAE gaps become accessible, as in tokamaks, and the transition from GAE to TAE modes could be observed [2].

The low-frequency coherent Alfvén modes do not cause significantly increased losses. These modes are typically observed under conditions with $v_A > v_{beam}$, where only sideband excitation is possible. With increasing beam power and density, however, strong bursting mode activity occurs with frequencies up to 500 kHz, which can induce significant energy and particle losses [4,5]. Occasionally strong frequency chirping is observed, indicating nonlinear interactions with resonant fast particles. The onset of these modes coincides in many cases with the decay of the Alfvén speed below the maximum fast particle velocity, and therefore additional modes can be excited. The analysis of the mode structure was not possible experimentally in the high-frequency range, but the observed phenomena seem to be consistent with higher order global Alfvén modes or kinetic ballooning modes. As an example of the correlation between such mode activity and confinement properties, some global plasma parameters are shown in Fig. 2 with a wavelet spectrogram of a Mirnov signal.

Further studies, particularly in the high-frequency range, are necessary to assess the potential effects of these modes on the confinement of fast particles in larger machines such as W7-X.

Arthur Weller, Caio Görner, Mathias Anton, Joachim Geiger,
Carolin Nührenberg[1]
Max-Planck-Institut für Plasmaphysik
EURATOM Association
D-85748 Garching, Germany
[1]D-17489 Greifswald, Germany

References

[1] D. A. Spong et al., in *Proc. 15th IAEA Conf. Plasma Phys. Controlled Nuclear Fusion Research* (Seville, 1994), Vol. 3, IAEA, Vienna (1996) 567.

[2] C. Nührenberg et al., Stellarator News, this issue.

[3] C. Görner et al., “Computational study of toroidal Alfvén eigenmodes in W7-AS,” *Stellarator News,* Issue 55, January 1998.

[4] C.Y. Teo et al., Nucl. Fusion **38**, 409 (1998).

[5] A. Weller et al., paper IAEA-F1-CN-69/EX2/1 presented at the 17th IAEA Fusion Energy Conference (Yokohama, 1998), to be published in the proceedings.

Island divertor studies for W7-AS

In optimized low-shear stellarators such as W7-AS and W7-X the configurations are bounded by an inherent chain of macroscopic magnetic islands which can be used, together with adequately arranged target plates and baffles, to form an intrinsic island divertor [1]. The plasma diffusing across the last closed flux surface (LCFS) enters the island regions and is directed to the targets located at the rear of the islands.

In 1999 the poloidal inboard limiters on W7-AS will be replaced by ten symmetrically arranged divertor targets and baffles very similar to those planned for W7-X [2]. The island divertor topology is three-dimensional (3-D). Besides the toroidal variation of the island shape, which affects the cross-field transport, discontinuous target plates imply a toroidal localization of recycling. In the target zone, the island scrape-off layer (SOL) is poloidally closed, which enables trapping of recycling particles between the separatrix and the targets. The trapping tends to raise the local density and hence to improve the decoupling of neutrals from the plasma core. The ionization power is supplied mainly by parallel heat conduction, leading to a toroidal drop of the island core temperature towards the recycling zones, which in turn results in an additional density rise inside the islands.

These effects are very sensitive to the ratio of the connection length to the distance of the targets from the LCFS, as this ratio directly controls the balance between parallel and cross-field thermal transport to the targets and hence the recycling activity in the islands. It can be optimized by varying the rotational transform and the currents of additional control loops, which directly change both the size and the internal field line pitch of the islands. To what extent high density in the island core may compensate for the crucially short radial distance between the targets and the LCFS (≈5 cm for W7-AS and 8 cm for W7-X, standard configuration) is one of the main questions to be addressed by the W7-AS divertor program.

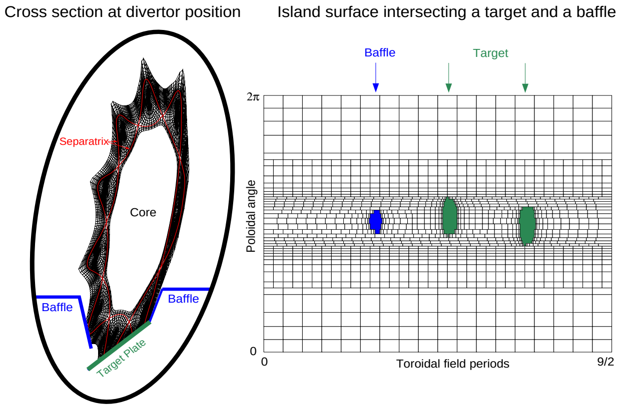

Fig. 1. 3-D grid for a 5/9 island divertor configuration in W7-AS. The grid is adjusted locally according to the required resolution.

The interpretation of the island divertor physics is more complicated than would be the case in a tokamak because of the island topology and the toroidal localization of targets and baffles. The divertor design for W7-AS has been supported by 2-D and 3-D edge transport modeling. The multifluid B2/EIRENE code [3,4] was adapted to the W7-AS island divertor configuration by helical averaging of the island configuration; this implies the assumption of continuous target plates [5]. Under these restrictions, the code has produced "proof-of-principle" predictions of high recycling and stable, layer-like detachment at the target plates in W7-AS, including radiation from sputtered carbon.

A realistic treatment of the island divertor geometry has become possible by the recent development of the EMC3 (**E**dge **M**onte **C**arlo **3**D) code [6]. This code solves a simplified set of time-independent Braginskii plasma fluid equations in three dimension (presently without impurities) and is coupled with the EIRENE code for the neutrals. The plasma and all relevant plasma-facing installations are modeled in their real 3-D geometry. High flexibility for resolving strongly diverted magnetic structures and high gradients near the targets is provided by a

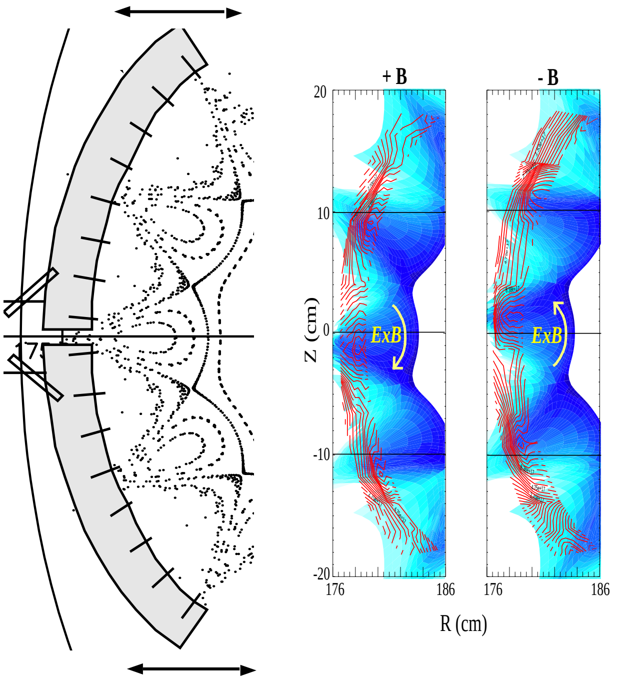

Fig. 2. Left: Langmuir probe array (movable) and vacuum island chain for a 5/9 configuration. Right: density distribution in the island region from probe data (red lines) and EMC3 code (blue shadows) for +*B* and −*B*. *The* poloidal asymmetry reverses with the *B*-field direction.

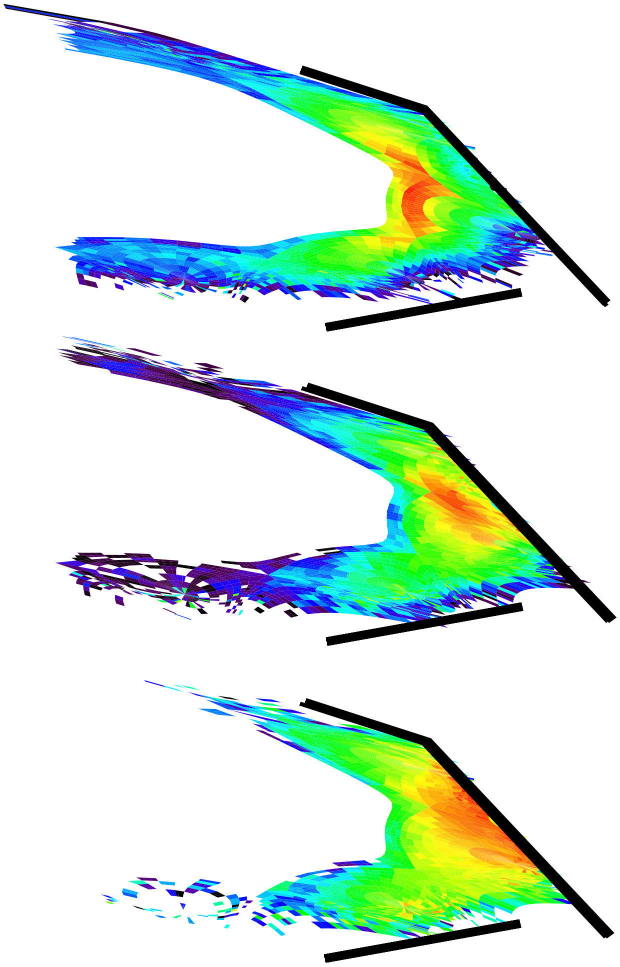

Fig. 3. Ion source distribution from an EMC3 code simulation in a divertor half cross section for three density values, increasing from top to bottom. The target plate and the two baffles are sketched.

locally adjustable, non-orthogonal grid (Fig. 1). After the fluid equations are represented in a Fokker-Planck form, they are solved with a common procedure by tracing Monte Carlo “particles” in magnetic coordinates. The code is fully parallelized.

The code was first applied to the present 5/9 island configuration of W7-AS with inboard limiters, for which it reproduced the measured transition from low to high recycling conditions, in particular the density peaking inside the islands from determined from Langmuir probe data and the steep rise of the H_α emission from the targets [2,7]. For low-density discharges, the EMC3/EIRENE code could also reproduce typical B-direction-dependent, poloidal asymmetries of the plasma density distribution inside the islands, as measured by a Langmuir probe array (Fig. 2). The asymmetries were simulated by superimposing an $\boldsymbol{E} \times \boldsymbol{B}$ drift associated with a radial T_e drop inside the islands towards the O-point [8].

Compared to tokamaks, the small poloidal and radial extent of the divertor region in W7-AS leads to stronger contributions from cross-field transport of particles, momentum, and energy. In particular, the EMC3/EIRENE code predicts strong momentum losses arising from the viscous radial coupling of particles flowing in opposite directions along adjacent island fans. These losses lead to an additional parallel pressure drop, even for low recycling, comparable to that due to plasma-neutral charge exchange interaction for high recycling conditions [6].

Recently the code has been applied to high-density “detachment-like” conditions with temperatures down to 1 eV at the targets. Figure 3 shows how the ionization front shifts from the target towards the separatrix as the upstream density increases, indicating a gradual detachment.

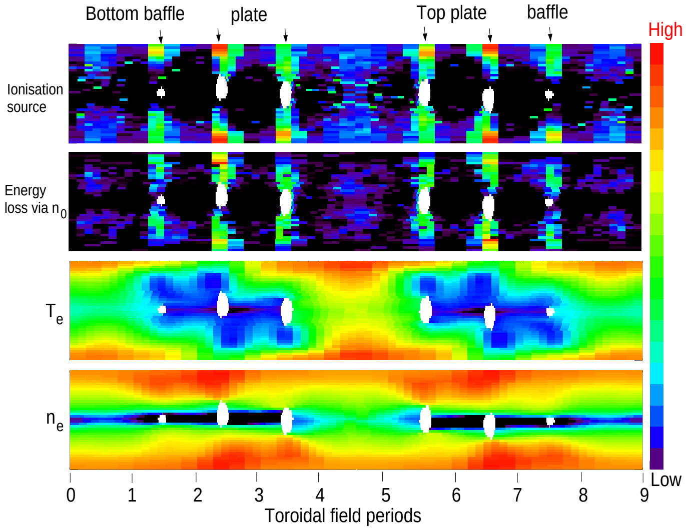

Fig. 4. Distributions of ion source, energy sink by neutrals, temperature, and density from EMC3 code simulation along an island tube over the full poloidal angle and the full helical periodicity of nine field periods. The island tube is cut by each target plate at two adjacent field periods.

In the detached case, the toroidal localization of the recycling zones leads to a strong toroidal inhomogeneity of the downstream plasma parameters. This is illustrated in Fig. 4, which shows the distributions of ion source, energy sink by neutrals, temperature, and density along an island tube cut by the target plates. In the recycling regions, an extended cold plasma zone is established over the full radial range of the SOL, over the full poloidal angle, and toroidally over two field periods. The previously mentioned temperature drop and density rise towards the recycling zone are particularly pronounced in the poloidal zones opposite the target positions, where the density and temperature profiles along the island tube are clearly phase shifted to each other. Inclusion of impurity transport and radiation is under way.

Y. Feng, F. Sardei, P. Grigull, J. Kisslinger
Max-Planck-Institut für Plasmaphysik
EURATOM Association
D-85748 Garching, Germany
E-mail: sardei@ipp.mpg.de
Phone: +49-89-3299-1369

References

[1] J. Kisslinger et al., in *Proc. 21st EPS Conf. Controlled Fusion Plasma Phys.* (Montpellier), **18B**, Part I, p. 368.

[2] F. Sardei et al., J. Nucl. Mater. **241–243**, 135, (1997).

[3] B. J. Braams, Report No. (NET) EUR-FU/XII-80/87/68, EC, Brussels, 1987.\; R. Schneider et al., J. Nucl. Mater. **196–198**, 810 (1992).

[4] D. Reiter, Report No. 2599, Institut für Plasmaphysik, Association EURATOM-KFA, Jülich, 1992.

[5] G. Herre et al., in *Proc. 13th Intern. Conf. on Plasma-Surface Interactions*, San Diego, USA,1998, to be published in *J. Nucl. Fusion.*

[6] Y. Feng at al., Proc. 13th Int. Conf. Plasma-Surface Interactions (San Diego, 1998), to be published in *J. Nucl. Fusion*.

[7] P. Grigull et al., J. Nucl. Mater. **241–243**, 935(1997).

[8] Y. Feng et al., in *Proc 24th EPS Conf. Controlled Fusion and Plasma Physics* (Berchtesgaden, 1997), Europhys. Conf. Abstr. **21A**, IV, p. 1569.+

Quasisymmetries in toroidal confinement

Particles in toroidal plasmas with parameters typical of fusion performance have extremely long mean free paths between collisions, typically a thousand times longer than the torus circumference. Therefore, an important aspect of toroidal plasma confinement is collisionless magnetic confinement of particle orbits. The magnetic moment of a particle, which is related to its fast gyromotion, is an adiabatic invariant, and the motion of the center of the gyrocircle is called the guiding center orbit.

Together with energy conservation in a static magnetic field, this invariant causes the reflection of particles which move into a region of increasing field strength for particles with sufficiently small velocities parallel to the magnetic field. This leads to the trapping of particles between regions of large field strength (the magnetic mirror effect). In addition, guiding center orbits experience drifts perpendicular to field lines due to field strength gradients and field line curvature. Collisions being rare, these two effects together will — in general, for arbitrary toroidal confinement regions —cause both direct collisionless particle loss of high-energy, e.g., alpha particles and large diffusion coefficients of thermal particles.

If the confinement domain exhibits a continuous symmetry — in a torus, this is the axisymmetry about the major torus axis with the toroidal angle the ignorable coordinate — an additional constant of motion arises and prevents collisionless orbit loss. If the confinement region could be straight, two additional symmetries would exist: axisymmetry about the axis of the plasma column (“poloidal” symmetry) and helical symmetry. With the necessity of a toroidal confinement domain (because of the intolerable end losses of a long but finite plasma column) these latter symmetries do not seem to be accessible. However, when the motion of guiding centers is described in coordinates especially adapted to the geometry of magnetic field lines (“magnetic” coordinates, in which field lines appear straight) it turns out that guiding centers do not experience the full geometrical properties of a confining magnetic field. The only three-dimensional (3-D) function entering their equations of motion in these coordinates is the magnetic field strength; the flux-surface shape and other geometrical properties do not enter.

So, an apparently counterintuitive question arises: whether the field strength of a nonaxisymmetric, i.e., genuinely 3-D, toroidal confinement domain can exhibit one of the three symmetries described above in this special representation. In essence, the answer is affirmative for the cases of axisymmetric and helically symmetric topographies of the field strength. Confinement configurations of these types

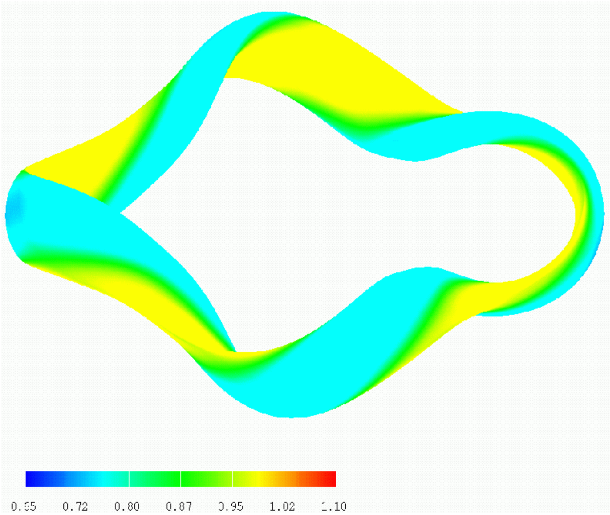

Fig. 1. A quasihelically symmetric stellarator with four periods. Shown is the field strength *B* (blue = low field, yellow = high field) on the plasma boundary. Note the helical structure of *B* overriding the effect of toroidal curvature. Reflected particles drift helically.

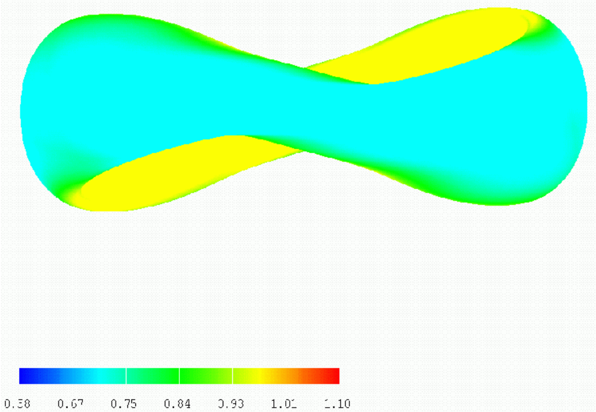

Fig. 2. A quasiaxisymmetric stellarator with two periods. Even though the geometry is strongly three-dimensional, reflected particles drift toroidally.

are named quasisymmetric, since the symmetry does not pertain to the geometry itself.

Quasipoloidal symmetry cannot be realized, but this fact led to the recognition that it would be sufficient to prevent orbit loss of an ersatz particle more sophisticated than the guiding center particle. In connection with the trapping of particles between hills in the magnetic topography, a second adiabatic invariant arises: the action integral between reflection points. Therefore, it suffices to have the contours of this second invariant poloidally closed. Confinement configurations of this type exist and are named quasiisodynamic because guiding centers would drift only in magnetic surfaces (and thus behave isodynamically) if quasipoloidal symmetry existed.

The relevance of these findings becomes apparent in considering the current state of knowledge on optimal toroidal fusion concepts: the most developed concept, the tokamak, cannot currently be unequivocally identified as optimal because of its problems with disruptions (nonlinear developments of instabilities leading to abrupt plasma termination) and the noninductive current drive necessary for stationary operation. On the other hand, the potential alternative for avoiding these problems, the stellarator, had been plagued by its inability — which had been deemed fundamental — to confine collisionless particles without strong radial electric fields.

With the results indicated above, three innovative lines of stellarator research have begun to be investigated. The discovery of quasihelically symmetric configurations [1] provided the first possibility of building a stellarator with collisionless particle confinement and led to the experimental realization (to be completed soon) of a small, university-scale device, the Helically Symmetric Experiment (HSX) at the University of Wisconsin (USA). Figure 1 shows the topography of *B* at the plasma boundary; the helical feature of this quantity is obvious. The concept of quasiaxisymmetry [2] allows the introduction into a tokamak-like (i.e., with significant toroidal current) configuration of externally created rotational transform (the helical twist of field lines as they go around the torus) without spoiling the particle confinement. This line, in which the danger of disruptions and the need for current drive may be mitigated, is being pursued with conceptual designs at the Princeton Plasma Physics Laboratory (USA) and the National Institute for Fusion Studies (Japan). Figure 2 shows the geometry and magnetic topography exhibiting the axial feature. The third confinement principle, quasiisodynamicity [Editor’s note: also called quasiomnigeneity] [3], is being realized in Wendelstein 7-X, a medium-sized superconducting device designed for stationary operation being built by the Max-Planck-Institut für Plasmaphysik in Greifswald. Wendelstein 7-X exhibits the quasiisodynamic confinement feature at finite plasma beta, the ratio of plasma to magnetic field energy in the confinement domain. Figure 3 shows its geometry and magnetic topography, exhibiting the poloidal feature for particles reflected within a period.

The complex three-dimensional features of Figs. 1–3 show that the realization of these configurational types required extensive computational efforts (by the standards of computing powers available in the 1980s). They were connected to the development of the theoretical design [4] of Wendelstein 7-X as an optimized stellarator satisfying an essential set of physics goals to be met by a stellarator viable for fusion application. These requirements pertain to equilibrium, stability, and transport properties of high-

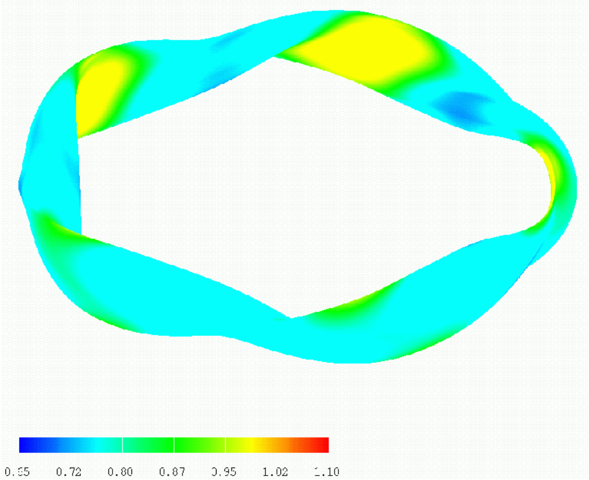

Fig. 3. The Wendelstein 7-X stellarator with five periods. Particles reflected within one period drift poloidally.

temperature toroidal plasmas, and it was shown that they are simultaneously satisfied in the W7-X configuration.

Essential elements of this optimization were (1) on the theoretical side, qualitative knowledge about geometrical features of stellarator configurations with beneficial influence on their confinement behavior; (2) on the computational side, the solution of non-linear but well-posed boundary value problems for describing stellarator configurations as a basic element used in a nonlinear optimization procedure; and (3) on the strategic side, a risk strategy for a hierarchical attainment of physics properties, namely elimination of candidate configurations with the help of that physical property that can most easily be shown to be not attained.

J. Nührenberg
Max-Planck-Institut für Plasmaphysik
Teilinstitut Greifswald
EURATOM Association
D-17489 Greifswald, Germany

References

[1] J. Nührenberg and R. Zille, Phys. Lett. A **129**, 113 (1988).

[2] J. Nührenberg, W. Lotz, and S. Gori, in *Theory of Fusion Plasmas*, (1994), 3; P.R. Garabedian, Phys. Plasmas **3**, 2483 (1996).

[3] S. Gori, W. Lotz, and J. Nührenberg, in *Theory of Fusion Plasmas* (1996), 335.

[4] W. Lotz, J, Nührenberg, and C. Schwab, in *Proc. 5th Conf. Plasma Phys. Contr. Nucl. Fusion Research* (Washington, 1990), IAEA, Vienna, Vol. 2, p. 603 (1991).

Design studies of low-aspect-ratio quasiomnigeneous stellarators

Configuration optimization

Development of increasingly sophisticated optimization methods in recent years [1–3] allows the design of stellarators that could lead to an attractive fusion power plant. Improved plasma confinement is achieved either through targeting symmetries (e.g., either helical [4] or toroidal [5]) of $|\boldsymbol{B}|$ in Boozer magnetic coordinates [6] or by directly attempting to reduce the deviation of particle guiding-center orbits away from flux surfaces [7]. Our stellarator optimization technique follows the latter approach, targeting the alignment of second adiabatic invariant J^* [8] contours for the trapped particle population with magnetic flux surfaces (known as QO or quasi-omnigeneity). As this optimization method has evolved, additional physics and engineering targets have been included, such as Mercier stability, rotational transform $\iota\!\!\!-(r) = 1/q$ in the range of 0.5 to 0.8 (with less than 30% of it due to plasma current), good coil realizability, low ripple, and ballooning and kink stability.

Our optimization is composed of (1) an adjustment of the outer magnetic surface shape and plasma current profile to achieve the desired physics goals, followed by (2) a synthesis of the modular magnetic coil geometry which produces that outer surface shape. Our earlier studies [1,2] produced low-aspect-ratio stellarator configurations that had promising features for a reactor (stable at $\langle\beta\rangle > 7\%$, low bootstrap current, and reasonable confinement), but they were not self-consistent or optimized for an experimental test at modest scale. With development of a modest experiment in mind, our recent QO optimizations have focused on $N_{fp} = 3$, 4 devices (N_{fp} = number of field periods) because they seem to provide a good compromise between the achievement of desired physics properties and simple coil configurations with adequate plasma/coil spacing. In this paper we analyze both $N_{fp} = 3$ ($R_0/a = 3.6$) and $N_{fp} = 4$ ($R_0/a = 4.2$) devices for the parameters of $R_0 = 1$ m, $B_0 = 1$ T. The $\iota\!\!\!-$ profile for $N_{fp} = 3$ varies from 0.55 to 0.64, while that for $N_{fp} = 4$ varies from 0.68 to 0.78. The flux surfaces for the $N_{fp} = 3$ device are shown in Fig. 1; the B_{mn} spectrum is shown in Fig. 2(a). The helical $m = 1$, $n = 1$ component is dominant, but not to the same degree as in a quasihelical device. There is a residual mirror field ($m = 0$, $n = 1$), which is the dominant component in W7-X [3]. The present configurations arose from a large-R_0/a (> 5), nearly quasihelical state, by reducing R_0/a while trying to retain $J^* = J^*(\psi)$. Trapped particle orbits approximately follow the J^* contours [Fig. 2(b)] in their bounce precessional motion; our optimization

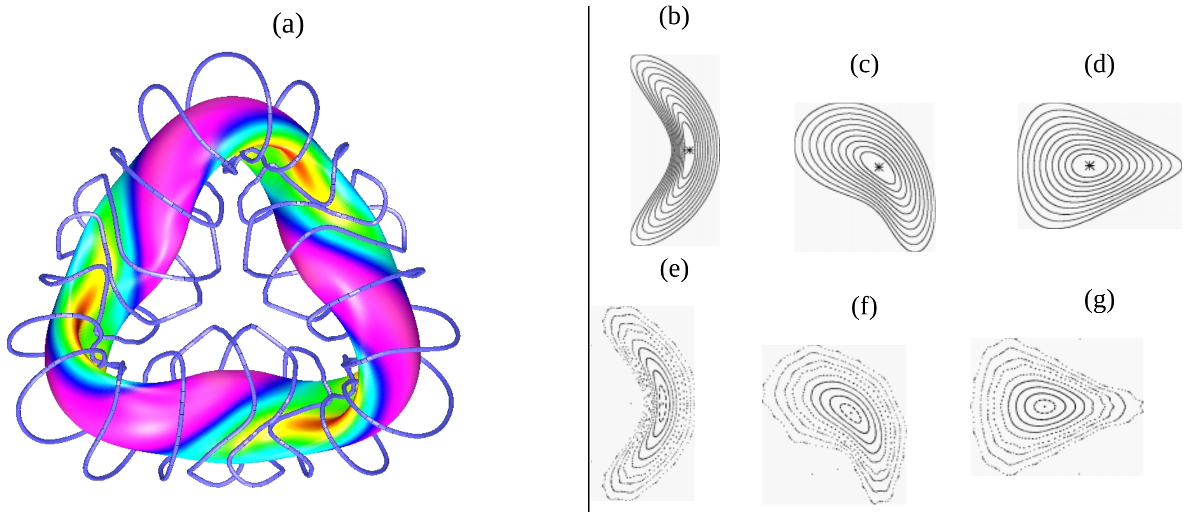

Fig. 1. (a) Outer flux surface and modular coils for an N_{fp} = 3 QO device. (b)–(d) VMEC flux surfaces for this configuration at toroidal angles ζ/N_{fp} = 0×, 90×, and 180×. (e)–(g) Flux surfaces reconstructed from following field lines based on the modular coil configuration at ζ/N_{fp} = 0°, 90°, and 180°.

attempts to make the J^* contours over a range of ε/μ values as nearly circular and closed as possible.

Neoclassical transport

The QO optimization technique is expected to lead directly to reductions in neoclassical transport because cross-field drifts scale with $<\mathbf{v}_D \cdot \nabla\psi> \propto \partial J^*/\partial\theta$. While empirical transport scalings such as ISS95 [9] may be expected for a QO experiment, it is desirable to minimize neoclassical transport well below this level so that any enhanced confinement regimes will lead to a measurable improvement. In Fig. 3(a) we plot the density dependence of the Monte Carlo particle diffusion coefficient for N_{fp} = 3 and 4 devices. These have been calculated using 2000 particles at zero ambipolar electric field and a constant plasma temperature of 1 keV (the test particles are monoenergetic at 2 keV). The diffusivities show a drop-off with decreasing collisionality without evidence of a ripple-induced (i.e., $1/\nu$) scaling. By calculating a sequence of such monoenergetic diffusivities over a range of energies, we integrate to obtain the transport coefficients for a Maxwellian distribution. This has been carried out for the N_{fp} = 4 device at a density of 5×10^{13} cm^{-3} and as a function of the ambipolar electric field. Using this sequence, we obtain the heat conductivity by taking the energy moment [Fig. 3(b)]. The 0-D energy confinement time $\tau_E \approx a^2/4\kappa$ is plotted based on this heat conductivity. For comparison, the empirical ISS95 lifetime $\tau_{E,\text{ISS95}}$ = 11.4 ms (based on an enhancement factor H = 2) for these parameters (B = 1 T, $\langle a \rangle$ = 0.23 m, $n = 5 \times 10^{13}$cm ^{3}, P = 2 MW) roughly equals the neoclassical confinement time in the absence of an electric field. Ambipolar electric fields in the range $e\phi/kT_{\text{ion}}(r = a) \approx 2$ to 3 are expected where, from Fig. 3(b), $\tau_{E,\text{neo}} = (2\text{–}3)\tau_{E,\text{ISS95}}$.

Energetic particle confinement and heating

The ability to heat toroidal plasmas depends critically on the confinement of energetic tail populations, which is a major motivation for our confinement optimization. We have particularly focused on the confinement of trapped

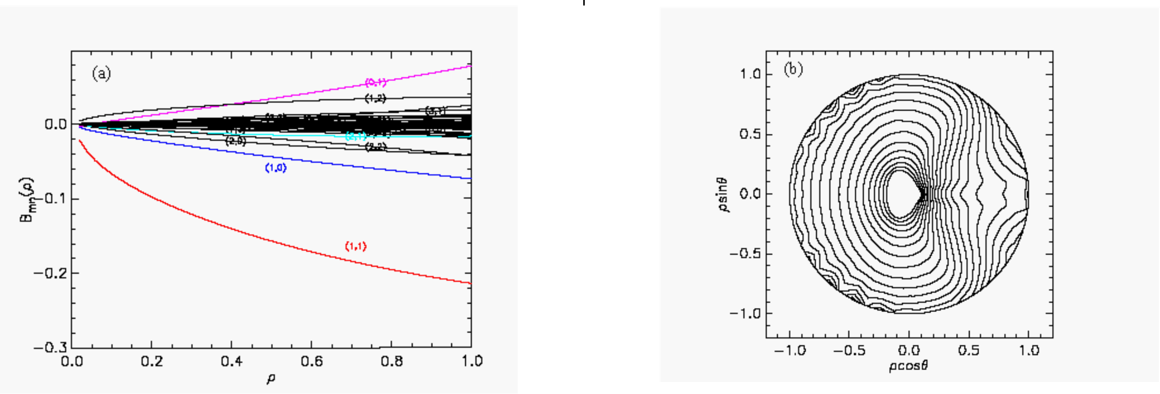

Fig. 2. Left: B_{mn} profiles for an N_{fp} = 3, R_0/a = 3.6 device. Right: J^* contours for trapped particles (ε/μ ~ 1.0 T) for the same device.

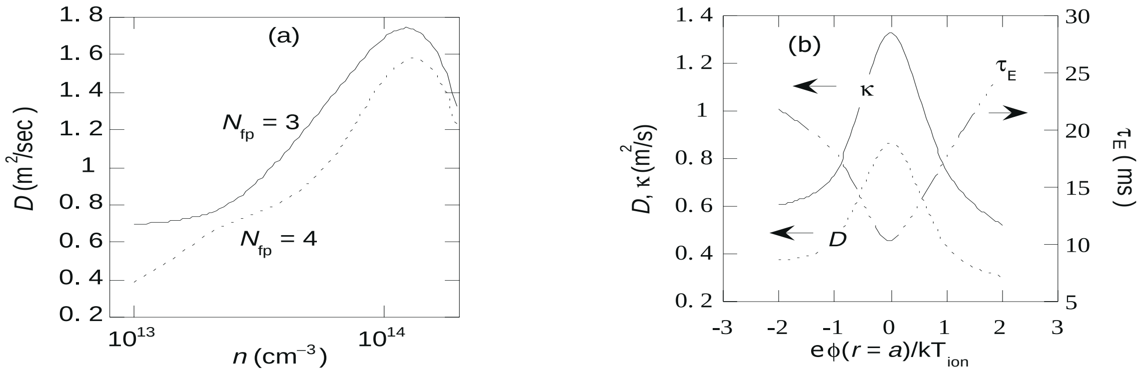

Fig. 3. (a) Density scaling of neoclassical diffusion coefficient based on monoenergetic Monte Carlo calculation. (b) Electric field scaling of neoclassical diffusion, heat conductivity and 0-D energy lifetimes (τ_E) for a Maxwellian distribution.

energetic ions that would be produced by ICRF heating. We have examined the confinement of this population by following an ensemble of collisionless particles and recording their loss rates vs time. All particles are launched at a specified energy at resonant locations where $B = B_{\text{resonant}}$ with $\varepsilon/\mu = B_{\text{resonant}}$ [i.e., the particles have their turning points ($v_{||} = 0$) at the resonant field]. Orbit losses occur both from open J^* contours and from deviations of the guiding center orbits away from the J^* surfaces. These orbit deviations are proportional to the particle's drift per bounce, which scales as ρ/a, the ratio of the gyroradius to the minor radius. In Fig. 4(a) we show results from following about 500 collisionless ions at 20 keV for flux surfaces in the inner 50% of the minor radius in our $N_{\text{fp}} = 4$ configuration. We vary the resonant field B_{resonant} from 0.9 T up to 1.15 T. This selects different starting locations for the ions as well as different values of ε/μ (and thus different J^* contours). Confinement depends sensitively on the value of B_{resonant}. This dependence arises from the variation of the J^* contours as ε/μ is changed. For $\varepsilon/\mu < 1$ T the J^* contours are relatively well closed, whereas for 1.05 T < ε/μ < 1.15 T there begin to be open contours which cause prompt particle losses. The dashed line in Fig. 4(a) indicates the rate at which a 20-keV ion collisionally slows down in a $T_e = 1$ keV background plasma; for the better confined cases, the particle loss approximately parallels the slowing-down rate, implying effective ICRF heating at these resonances. The other parameter which influences ion confinement is ρ/a; this determines the degree to which the particle orbit deviates from constant J^* contours. Increasing the magnetic field from 1 to 2 T uniformly improves energetic particle confinement for both $N_{\text{fp}} = 3$ and 4 devices. We have applied this calculation to the CHS configuration ($N_{\text{fp}} = 8$) in which ICRF heating has been used. We find that the confinement in our configurations generally exceeds that calculated for CHS, leading us to conclude that trapped ion confinement should be adequate for ICRF heating.

We have also scaled these configurations to reactor sizes ($B_0 = 5$ T, $R_0 = 10$ m) to check alpha particle confinement [Fig. 4(b)]. These calculations are based on following a group of about 500 collisionless alpha particles ($E_0 = 3.5$ MeV) born at $r/a = 0.25$. The impact of these levels of alpha particle losses is not expected to be a major issue for the power balance, but will need further analysis with respect to localization of power loading on the first wall.

Stability

Our optimization procedure checks for the existence of a magnetic well, in addition to favorable Mercier and ballooning stability over the whole plasma radius. Ballooning β thresholds for the $N_{\text{fp}} = 3$ and 4 configurations discussed above are approximately 2% and 2.5%, respectively, which is adequate for a test in a modest experiment. Typically, for broad pressure profiles, a region near the edge goes unstable first. Several methods have been successfully used in our previous configurations to extend the stable window into the $\langle\beta\rangle = 5$ to 6% range, including profile flattening, increased shear in the ɫ profile, and boundary shaping. A fast hybrid finite difference/variational version of the ballooning calculation has recently been developed and should facilitate improved optimization of the ballooning stability limit. In addition, low-n pressure-driven instabilities have been analyzed with a 3-D initial value MHD model [10]. The low-n radial mode structure shows structure similar to the radial dependence of the high-n ballooning growth rate.

Bootstrap current

The rotational transform for the configurations presented here is predominantly produced by plasma shaping; the bootstrap current typically provides ≤12% change in ɫ for $\langle\beta\rangle$ up to 3%. Our optimization procedure currently does not self-consistently include the bootstrap current, but sensitivity studies have been made outside the optimization loop of the effect of different levels and directions of bootstrap current. We find that our configurations are relatively

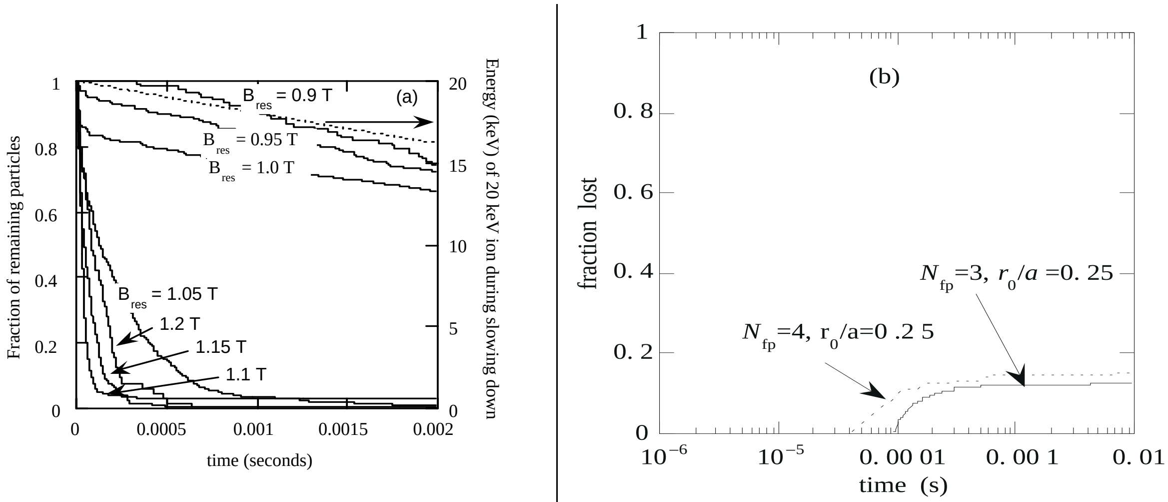

Fig. 4. (a) Fraction of 20-keV ICRF resonant ions confined vs time for an N_{fp} = 4 device (B_0 = 1 T), for different values of $\varepsilon/\mu = B_{res}$. (b) Fraction of 3.5-MeV alpha particles lost vs time for reactor-scale versions of the N_{fp} = 3 and 4 devices, starting particles at r/a = 0.25.

robust to such changes. The degree of omnigeneity is not strongly affected nor is the transform profile changed significantly, especially for the ranges of $\langle\beta\rangle$ (i.e., 1–2%) which would characterize a near-term experiment. However, in order to better control these effects and to ensure that the transform profile has the appropriate sign of shear to prevent the growth of neoclassical bootstrap current-driven islands, we expect in the near future to include these effects directly in our optimization method.

Conclusions

We have studied a range of attractive low-field-period (N_{fp} = 3 or 4) devices for testing the QO optimization technique. Our method targets improvements in energetic particle confinement, core transport, stability, ease of coil design, and low aspect ratio. Modular coil sets exist which produce our optimized systems and these preserve both the original flux surfaces and the optimized physics properties. This optimization effort is ongoing, and we expect to further address such issues as ballooning stability optimization, self-consistent bootstrap current, and a more comprehensive modeling of transport and ICRF heating.

D. A. Spong, S. P. Hirshman, J. C. Whitson, D. B. Batchelor,
R. Sanchez, B. A. Carreras, V. E. Lynch, J. F. Lyon, P. M. Valanju,[1] W. Miner,[1] P. Moroz,[2] M. C. Zarnstorff,[3] D. A. Monticello,[3]
A. S. Ware,[4] L. Garcia[5]
Oak Ridge National Laboratory
P. O. Box 2009
Oak Ridge, Tennessee 37831-8071
[1] University of Texas, Austin, Texas
[2] University of Wisconsin, Madison, Wisconsin
[3] Princeton Plasma Physics Laboratory, Princeton, New Jersey
[4] University of Montana, Missoula, Montana
[5] Universidad Carlos III de Madrid, Madrid, Spain

Acknowledgment

This research was sponsored by the Office of Fusion Sciences U.S. Department of Energy, under contract DE-ACO5-960R22464.

References

[1] S. P. Hirshman, et al., Phys. Rev. Lett. **80**, 528 (1998).

[2] D. A. Spong et al., Phys. of Plasmas **5**, 1752 (1998).

[3] S. Gori et al., in Theory of Fusion Plasmas (Varenna, 1996), Editrice Compositori, Bologna (1997) 335.

[4] J. Nührenberg and R. Zille, Phys. Lett. **A129**, 113 (1988).

[5] P. R. Garabedian, Phys. Plasmas **3**, 2483 (1996).

[6] A. H. Boozer, Phys. Fluids **23**, 904 (1980).

[7] J. R. Cary et al., Phys. Rev. Lett. **78**, 674 (1997); see also A. A. Skovoroda et al., Plasma Phys. Rep. **21**, 937 (1995), and H. Weitzner, Phys. Plasmas **4**, 575 (1997).

[8] J. A. Rome, Nucl. Fusion **35**, 195 (1995); also, J. R. Cary et al., J. Phys. Fluids **31**, 1586 (1988).

[9] U. Stroth et al., Nuclear Fusion **36**, 1063 (1996).

[10] L. Garcia, R. Sanchez, and J. A. Jimenez, J. Plasma Fusion Res. Series **1**, 468 (1998).